Hydrothermal trace metal release and microbial metabolism in the Northeast Lau Basin of the south Pacific Ocean

Natalie R. Cohen[1,2], Abigail E. Noble[1], Dawn M. Moran[1], Matthew R. McIlvin[1], Tyler J. Goepfert[1,3], Nicholas J. Hawco[4], Christopher R. German[1], Tristan J. Horner[1], Carl H. Lamborg[5], John P. McCrow[6], Andrew E. Allen[6], and Mak A. Saito[1]

[1] Woods Hole Oceanographic Institution, Woods Hole MA 02543 USA
[2] University of Georgia Skidaway Institute of Oceanography, Savannah GA 31411 USA
[3] Arizona State University, Tempe AZ 85281 USA
[4] University of Hawai'i at Mānoa, Honolulu HI 96822 USA
[5] University of California, Santa Cruz, Santa Cruz, CA 95064 USA
[6] J. Craig Venter Institute, La Jolla CA 92037 USA

Correspondence to: Natalie R. Cohen (cohen@uga.edu) or Mak A. Saito (msaito@whoi.edu)

Abstract. Bioactive trace metals are critical micronutrients for marine microorganisms due to their role in mediating biological redox reactions, and complex biogeochemical processes control their distributions. Hydrothermal vents may represent an important source of metals to microorganisms, especially those inhabiting low iron waters, such as in the southwest Pacific Ocean. Previous measurements of primordial ^{3}He indicate a significant hydrothermal source originating in the Northeast (NE) Lau Basin, with the plume advecting into the southwest Pacific Ocean at 1,500-2,000 m depth (Lupton et al. 2004). Studies investigating the long range of trace metals associated with such dispersing plumes are rare, and the biogeochemical impacts on local microbial physiology have not yet been described. Here we quantified dissolved metals and assessed microbial metaproteomes across a transect spanning the tropical and equatorial Pacific with a focus on the hydrothermally active NE Lau Basin, and report elevated iron and manganese concentrations across 441 km of the southwest Pacific. The most intense signal was detected near the Mangatolu Triple Junction (MTJ) and Northeast Lau Spreading Center (NELSC), in close proximity to the previously reported ^{3}He signature. Protein content in distal plume-influenced seawater, which was high in metals, was overall similar to background locations, though key prokaryotic proteins involved in metal and organic uptake, protein degradation and chemoautotrophy were comparatively abundant compared to deep waters outside of the distal plume. Our results demonstrate that trace metals derived from the NE Lau Basin are transported over appreciable distances into the southwest Pacific Ocean, and that bioactive chemical resources released from submarine vent systems are utilized by surrounding deep sea microbes, influencing both their physiology and their contributions to ocean biogeochemical cycling.

1 Introduction

The central Pacific Ocean encompasses several biogeochemical regimes, including low nitrate surface waters in the subtropical gyres, and high-nitrate, yet low-iron waters in the equatorial upwelling zone (Saito et al. 2014; Cohen et al. 2021). Towards the south Pacific Ocean, little dust input from continental sources combined with low macronutrient concentrations results in

35   low primary productivity and reduced biological carbon export to the deep ocean (Jickells et al. 2005). In this region, active

hydrothermal venting may be an important source of trace metals, such as iron, to surrounding microorganisms.

Hydrothermal venting can arise wherever seawater percolating down into the seafloor intercepts strong geothermal gradients,

for example as imposed by magmatic activity in the upper ocean crust. Such systems can be associated with mid-ocean ridge

spreading centers, intra-plate volcanoes, convergent margins, subduction zones, island arc volcanoes and back-arc spreading

40   centers (German and Seyfried 2013; Beaulieu et al. 2013). High temperature fluids released from vents serve as sources of

dissolved elements by enriching seawater in metals derived from the underlying crust. The chemicals most concentrated in

vent fluids, including iron (Fe), manganese (Mn), zinc (Zn), copper (Cu), methane and sulfides, reach mM to μM

concentrations compared to the pM to nM range typical of background seawater, and are used as energy sources for

chemosynthetic microbial communities that sustain rich food webs (Bruland and Lohan 2003; Tivey 2007). A substantial

45   portion of these hydrothermally-released trace metals rapidly precipitate as mineral sulfides and oxides through abiotic and

biological oxidation (Gartman and Findlay 2020). The hydrothermal fluid mixes with cool, oxidizing seawater and rises to

form buoyant plumes above vent sources. Once the buoyant plumes reach neutral density in the water column, they are spread

laterally by prevailing deep sea currents, transporting chemical resources and microbial communities into the deep ocean

interior in non-buoyant plumes (Dick et al. 2013; Reed et al. 2015). Trace metal concentrations within these plumes generally

50   decrease with distance from the hydrothermal source as a result of dilution and removal processes that include both abiotic

precipitation and microbial uptake (Cowen et al. 1990; Gartman and Findlay 2020).

However, recent observations demonstrate that detectable levels of metals such as Fe can be transported substantial distances

from vent sources, with both dissolved and particulate hydrothermally-sourced Fe released from the southern East Pacific Rise

traveling thousands of km west across the Pacific Ocean, tracking with primordial [3]He released from the mantle during

55   hydrothermal venting (Fitzsimmons et al. 2014, 2017; Resing et al. 2015). The Fe isotopic composition of central Pacific

seawater furthermore indicates that such distal transport of hydrothermal Fe has likely persisted over the Cenozoic (Horner et

al. 2015). Non-buoyant plume Fe is thought to be stabilized in the dissolved state as inorganic metal oxides, organic/inorganic

colloids, and through organic ligand complexation (Bennett et al. 2008; Fitzsimmons et al. 2014, 2017; Gartman and Findlay

2020). The next largest [3]He signal in the Pacific Ocean after the southern East Pacific Rise is associated with the Lo'ihi

60   Seamount system, which similarly produces a strong distal Fe plume (Jenkins et al. 2020). It remains to be determine whether

trace metals are similarly advected from the Northeast Lau (NE) Basin, where the third largest hydrothermal [3]He signal in the

Pacific Ocean has been measured, extending 2,000 km to the northwest and representing the most intense hydrothermal [3]He

signature in this ocean basin at ~1,700 m depth (Lupton et al. 2004; German et al. 2006).

The Northeast (NE) Lau Basin is a dynamic back-arc spreading region surrounded by plate boundaries in the tropical southwest

65   Pacific that contains an abundance of hydrothermal vent fields (Martinez et al. 2006; Beaulieu et al. 2013; Baker et al. 2019).

The basin is topographically restricted by the Lau and Tonga Ridges, which converge to the South (Speer and Thurnherr 2012).

Consequently, deep hydrothermal plumes can only escape the Lau Basin from the North, exiting into the southwest Pacific (German et al. 2006; Speer and Thurnherr 2012). The contributions of the prominent hydrothermal plume located off the Tonga Ridge (15°S and 173.1°W) to metal biogeochemistry and microbial physiology has yet to be investigated. In addition to its

70 unique geophysical properties, the NE Lau Basin contains mineral deposits of commercial interest. The hydrothermal sulfides from this region contain the highest gold contents on record (Herzig et al. 1993) and with plans ongoing to mine cobalt and nickel-rich ferromanganese nodules from the seafloor to meet increasing economic demands (Lusty and Murton 2018).

Recent observations indicate that in addition to distal hydrothermal plumes introducing a flux of chemically reduced elements and compounds to the ocean interior, these systems may impact metal availability to surface phytoplankton. The oligotrophic

75 south Pacific has extraordinarily low levels of continentally derived Fe and low macronutrient concentrations, resulting in nitrate and Fe limitation of phytoplankton growth (Jickells et al. 2005, Sunda et al. 2012, Behrenfeld et al., 2006). Hydrothermally-sourced, distally-transported Fe from the southern Eastern Pacific Rise and Loʻihi distal plume systems may eventually upwell to fertilize surface phytoplankton communities in the Southern Ocean and the subpolar North Pacific, respectively (Resing et al. 2015; Jenkins et al. 2020). Distally-transported Fe from the NE Lau Basin is therefore not only

80 critical to consider in the aphotic ocean; it could contribute euphotic zone primary production depending on water mass circulation and upwelling dynamics (Tagliabue et al. 2010; Jenkins et al. 2020).

Trace metal transformations in hydrothermal plumes are heavily driven by biological communities (Toner et al. 2009, 2016; Gartman and Findlay 2020). Prior microbiological and meta-ʻomic studies have offered insights into plume microbial community dynamics, with many studies focusing on near-field ecosystems (Jeanthon 2000; Huber et al. 2007; Takai et al.

85 2008; Sylvan et al. 2012; Li et al. 2014; Reveillaud et al. 2016), and fewer, more recent explorations into distal plumes (Djurhuus et al. 2017; Haalboom et al. 2020; Li et al. 2020). Microbial communities in plumes may be sourced from seafloor vent sites themselves, or seeded from background seawater (Dick et al. 2013; Reed et al. 2015; Sheik et al. 2015). They include members of the *Gammaproteobacteria*, *Thaumarchaea*, and *Deltaproteobacteria* (Dick et al. 2013; Anantharaman et al. 2016), with these groups decreasing with distance from the vent source (Haalboom et al. 2020). Chemosynthetic bacteria in

90 hydrothermal plumes carry out sulfur, methane, ammonia, hydrogen and manganese (Mn) oxidation, sharing functional characteristics with microbes from other reducing habitats (Dick et al. 2013; Anantharaman et al. 2016). The less frequently studied hydrothermal microeukaryote populations include archaeplastids, ciliates, dinoflagellates, rhizaria, and fungi, which have been identified based on partial metagenome-assembled genomes (Anantharaman et al. 2016), and are hypothesized to play a role in plume dissolved organic carbon cycling via grazing on chemosynthetic primary producers (Bennett et al. 2013).

95 Microbial community dynamics, ecology and biogeochemical contributions are comparatively less studied in distal

hydrothermal plumes due to their more recent characterization and fewer interdisciplinary expeditions where both the geochemistry and microbial ecology of ecosystems are considered.

The 2011 Metzyme expedition embarked across the central Pacific Ocean with the goal of connecting trace element distributions with protein metabolism, and a suite of biological and physiochemical parameters were collected along vertical
100 and lateral ocean gradients (Saito et al. 2014, 2015, 2020; Munson et al. 2015; Santoro et al. 2017; Hawco et al. 2020; Cohen et al. 2021). The trace metal profiles across this section of the Pacific Ocean, and the sources and sinks driving their distributions, have not yet been described. In this study, we present the full-depth dissolved trace metal section and leverage the Metzyme protein dataset to address whether hydrothermal activity previously measured in the northeastern edge of the Lau Basin is associated with trace metal input, and determine whether surrounding microbes were sensitive to distal hydrothermal
105 plume geochemistry. Our results indicate several hydrothermal features based on dissolved iron and manganese profile anomalies, with relatively abundant proteins related to protein folding, protease activity and metal transport in the vicinity of a hydrothermal plume. We posit these hydrothermal sources are a significant contributor to metal biogeochemistry and microbial physiology in the tropical southwest Pacific Ocean.

2 Methods

110 **2.1 Oceanographic sampling section and biomass collection**

Seawater sampling occurred during October 1-25 2011 onboard the R/V *Kilo Moana* during the Metzyme expedition (Saito et al., 2014). The meridional transect (17°N-15°S) began off the Hawaiian Islands and terminated in the Tonga-Fiji region (173.1°W) of the NE Lau Basin (Fig. 1). Biomass collection for metaproteomics were performed using battery-operated underwater McLane pumps (McLane Research Laboratories) outfitted with custom filter head units secured onto a trace metal
115 clean winch line. Each McLane pump head had three filter fractions for targeting specific size classes of the microbial community. For this analysis, we considered the 3–51 µm fraction containing eukaryotic protists and particle-associated and/or adsorbed bacteria, archaea and viruses. Pumps filtered between ~100-1,000 L, and once retrieved onboard were promptly sectioned for 'omic analyses (16S/18S rRNA, proteins) and frozen at -80°C (Table S1). Meta-'omics was performed across spatial and vertical gradients of the transect (Cohen et al. 2021).

120 **2.2 Trace metal analyses**

Seawater samples for trace metal analyses were collected using a trace metal clean rosette consisting of 12 ~8L X-Niskins on a trace metal clean Amsteel winch line (Saito et al. 2014). Two sets of 12 niskin bottles were used for full stations to allow simultaneous casting and processing. Following seawater collection, X-Niskins were brought into a fabricated shipboard class-100 clean room and pressurized with filtered high purity nitrogen gas. Seawater was filtered through 47mm 0.2 µm Supor
125 membranes to remove the particulate fraction, which was saved for the particulate metal analysis. HEPA filters were used to minimize particle contamination and trace metal clean approaches were used during filtration and sample handling procedures.

Prior to sample collection, polyethylene bottles were cleaned by soaking for 2 weeks in 10% HCl (Baker Analyzed ACS Reagent) and by rinsing with pH 2 HCl. Seawater was acidified to pH 1.8 using hydrochloric acid (Optima grade, Fisher Chemical), and samples were stored for 8 years before this dissolved trace metal analysis was conducted.

130 Seawater preconcentration was performed using an automated solid phase extraction system, seaFAST pico, run in offline concentration mode (Bown et al. 2017; Rapp et al. 2017; Jackson et al. 2018; Wilson et al. 2019; Wuttig et al. 2019). The seaFAST contains a Nobias-chelate PA1 resin column (ethylenediaminetriacete and iminodiacetate) suitable for the simultaneous preconcentration of several trace metals (Fe, Mn, Zn, Cu, Cd, Ni) with high sensitivity and quantitative recovery (Sohrin et al. 2008; Biller and Bruland 2012). Reagents consisted of a 4M ammonium acetate pH 6.0 buffer (Elemental

135 Scientific), a 1% nitric acid rinse solution (Optima grade, Fisher Chemical), 10% nitric acid elution acid (Optima grade, Fisher Chemical), and a second "internal standard" 10% nitric elution acid solution containing 10 ppb indium ([115]In; SPEX CertiPrep). Solutions were prepared with 18.2 Ω Milli-Q water (Millipore). Polypropylene conical tubes used in the auto sampler were HCl acid-soaked for one week and pH 2-rinsed prior to use. Acidified samples were preconcentrated using an initial volume of 30-33 mL and elution volume of 500 µL. The volume range is due to early samples being run with four 10-mL loop load

140 cycles (exactly 40 mL seawater as the initial volume). The seaFAST vacuum overflows the load loop, which resulted in only 3 mL remaining during the last 10 mL cycle, and a resulting concentration factor of 66X. All subsequent samples were run with 3 full 10 mL load cycles for a 60X concentration factor. Process blanks consisted of MilliQ HCl-acidified to pH 2 (Optima grade, Fisher Chemical), and were run alongside samples to account for background reagent and sample handling contamination.

145 Following offline seaFAST preconcentration, the multi-element quantitative analysis was performed using an iCAP Q inductively coupled plasma-mass spectrometer (ICP-MS; Thermo Scientific). Oxide interference on metal isotopes was minimized through the use of a cooled spray chamber and helium collision gas. Analytes were measured in single quadruple mode (kinetic energy discrimination [KED]). Concentrations of Fe, Mn, Zn, Cu, and Cd were determined using a six-point external standard curve with a multi-element standard (SPEX CertiPrep), diluted to range from 1-10 ppb in 5% nitric acid and

150 prepared using volumetric flasks. Indium (In) standards (SPEX CertiPrep) were similarly added to these standard stocks, diluted to 1, 2, 3, 4 and 10 ppb. Instrument injection blanks consisted of 5% nitric acid in Milli-Q. Standard curve R^2 values were ≥0.98 for the elements monitored.

Using this resin-based preconcentration method, recoveries have been demonstrated to be >98% (Biller and Bruland 2012). In this analysis, partial recoveries of metals from the resin column were calculated using the known amount of In added to elution

155 acid (10ppb) and In counts per second (cps) values measured in each eluted sample, in which run recoveries averaged 83 ± 9%. Since In was added in the elution acid, and not to the sample prior to preconcentration, this is considered a partial recovery. Dissolved metal concentrations (dTM [nM]) were calculated for each metal following Eq. (1):

$$dTM = \frac{M_{Sample}}{In_{Sample}} - \frac{M_{Process}}{In_{Process}} \times \frac{In_{Elution}}{M_{Slope}} \times \frac{V_{Eluted}}{V_{Original}}, \tag{1}$$

where M_{Sample} represents the metal cps in a given sample, In_{Sample} is the [115]In cps of the sample, $M_{Process}$ and $In_{Process}$ are the average metal and [115]In cps, respectively, of the pH 2 process blanks, $In_{elution}$ is the [115]In cps of the solution used to elute metals off the resin column, M_{slope} is the slope (cps/ppb) of metal M determined with the SPEX standards, $V_{Original}$ is the volume preconcentrated (30 or 33 mL), and V_{Eluted} is the final volume eluted (500 µL) for a 60 or 66X concentration factor.

Method accuracy and precision was assessed using the 2009 Geotraces coastal surface seawater (GSC) standard (n = 3; Table 1; Fig. S1), where estimated precision was 0.6% (Fe), 7.2% (Cu), 2.4% (Cd), 7.4% (Cd), and 2.1% (Mn) relative standard deviation (RSD). We observed higher variability among standard runs for Zn likely due to handling contamination, with 25.5% RSD. Internal consistency was achieved by running previously analyzed deep seawater (from St. 9 and St. 13) alongside samples to monitor seaFAST accuracy over time, and to account for newly made batches of reagents and resin columns. Samples showing poor indium recovery or appearing oceanographically inconsistent with adjacent seawater depths were subsequently re-run.

Table 1. Reference seawater comparisons using the 2009 Geotraces coastal surface seawater (GSC) standard.

Metal	This Study (n = 3) (nM)	Geotraces consensus (nM)
Fe	1.74 ± 0.01	1.56 ± 0.12
Zn	1.37 ± 0.35	1.45 ± 0.10
Cu	1.53 ± 0.11	1.12 ± 0.15
Cd	0.41 ± 0.01	0.37 ± 0.02
Ni	4.61 ± 0.34	4.5 ± 0.21
Mn	2.33 ± 0.05	2.23 ± 0.08

Our data showed a systematic Cu offset with concentrations that were 7-22% higher than consensus values (Table 1; Fig. S1). We are unsure if this is associated with a systematic offset with our method or with the emerging notion that Cu may be underestimated in prior consensus standard reporting. Cu speciation in known to include kinetically inert species (Kogut and Voelker 2003), which could be resistant to exchange with preconcentration resins. It is possible that our higher dCu concentrations are a result of long-term acidified storage (8 years), during which time strongly binding refractory organic complexes could degrade and increase labile Cu (Little et al., 2018). Dissolved Cu has been previously been reported as 3.1 nM in the deep southwest Pacific using Nobias-chelate PA1 resin (Takano et al., 2017), whereas the maximum raw dCu concentration we obtained in the southwest Pacific was approximately 4.2 nM. The exact mechanism behind these elevated Cu concentrations is unclear at present, and an intercalibration exercise within the trace metal community would be useful to further understand these offsets.

185   Laboratory blanks consisted of MQ acidified to a pH of 2 with Optima-grade HCl and were run alongside seawater samples (Table 2). Blanks reflect contamination added from reagents, seaFAST tubing, and laboratory/shipboard sample handling. MQ blanks showing pronounced Fe and/or Zn contamination were removed from the data set. The detection limit (LOD) was determined using 3X the standard deviation of the pH 2 blanks. In runs where only 1 MQ blank was used, the LOD could not be determined.

190

Table 2. SeaFAST blanks and limits of detection. Concentrations shown are averages across runs ± 1 standard deviation, with replicate MQ blank concentrations averaged within runs. The number of test sets (n) represents individual sample runs where blanks were preconcentrated alongside seawater samples and analyzed via ICP-MS. *For Zn, high MQ blanks were observed in 4 runs, and these values were excluded from the blank and LOD averages shown.

	Fe (nM)	Mn (nM)	*Zn (nM)	Cu (nM)	Ni (nM)	Cd (nM)
LOD (n=12)	0.08 ± 0.08	0.005 ± 0.006	0.54 ± 0.29	0.09 ± 0.20	0.03 ± 0.01	0.0008 ± 0.0005
MQ Blank (n=18)	0.11 ± 0.07	0.03 ± 0.10	0.37 ± 0.17	0.09 ± 0.16	0.05 ± 0.07	0.02 ±0.07

195

The seaFAST was used to quantify dissolved Fe, Mn, Zn, Cu, Ni and Cd. To accurately quantify Co, UV-oxidation is necessary to disrupt strong organic ligands associations, and irradiation was not performed on seaFAST-preconcentrated seawater samples. A substantial fraction of the total dissolved Co was strongly bound to organic ligands, unchelated by the Nobias resin, and lost during the preconcentration procedure (Saito and Moffett 2001, Billard and Bruland 2012, Milne et al. 2010, Ndung'u

200   et al 2003). Even when using UV-oxidation, the Nobias resin does not reproduce the full Co inventory and a fraction is lost. Instead, dissolved Co data was obtained using cathodic stripping voltammetry with seawater exposed to UV oxidation for 1 hour (Hawco et al. 2020).

Filter fractions for the particulate metal analysis were digested in 50% nitric acid and heated for 3 hours at 90°C, using 1 ppb

205   In as an internal standard, diluted with 5% nitric acid, and quantified on an Element2 ICP-MS alongside external SPEX standards (Goepfert 2013). Originally, blanks consisted of 0.2 µm Supor filters that were soaked in 10% HCl and rinsed with MQ until a neutral pH was achieved. These filters were not rinsed with ultra-filtered seawater. Metal contamination on these filter blanks was high, with metal counts orders of magnitude lower in all filters exposed to seawater. We suspect metals derived from the cleaning acid were retained on the filters and seawater conditioning/flushing would have reduced this

210   contamination. We instead calculate particulate metal concentrations by using pFe and pMn concentrations from 400m within an OMZ as a low metal reference "blank", which is a conservative approach and underestimates true particulate metal concentrations.

2.3 Metaproteomics

215 Biomass was collected onto 3-51 µm filters using *in situ* battery operated McLane pumps which filtered 165-1384 L of seawater over the course of several hours, with flow rate depending on the suspended load present (Table S1). Seawater was first passed through a 51 µm pre-filter to exclude multi-cellular organisms, aggregated colonies and large organic debris followed by 3 µm and 0.2 µm filter membranes to capture the microeukaryotic and prokaryotic communities. Filters were frozen at -80°C until laboratory extractions. Proteins were extracted following a sodium dodecyl sulphate (SDS) detergent-
220 based method to solubilize membrane and soluble proteins and heated for 10 mins at 95°C (Saito et al. 2014; Cohen et al. 2021). Protein quantification was performed using a colorimetric Bradford protein assay with the Bovine Serum Albumin standard and a Nanodrop spectrophotometer. Digestion was performed using trypsin at a trypsin:protein ratio of 1:20, and peptides were further purified using C18 Zip-tips. For the mass spectrometry analysis, peptides were diluted to 0.1 µg/µL and 2 µg was injected onto a Dionex Ultimate3000 RSLCnano HPLC system in 2-dimension active modulation mode coupled to
225 a Thermo Fusion Orbitrap mass spectrometer operating in data dependent acquisition mode (McIlvin et al. in prep). The mass spectrometer monitored MS^1 scans from 380-1580 m/z at 240K resolution and MS^2 scans had a 1.6 m/z isolation window, 50 msec maximum injection, and a 5 sec dynamic exclusion.

The translated metatranscriptome was used as the protein database (Cohen et al. 2021), and spectral matches were performed
230 using the SEQUEST algorithm within Proteome Discoverer using a fragment tolerance of 0.6 Da and parent tolerance of 10 ppm. Identification criteria consisted of a peptide threshold of 95% (1 peptide minimum) and protein threshold of 99% in Scaffold (version 4.8.4, Proteome Software Inc.). Exclusive spectral counts were normalized following the Normalized Spectral Abundance Factor (NSAF) approach. Open reading frames (ORFs) with a classified taxonomic annotation and lineage probability index greater than 0.7 were used for the downstream analysis. Annotations were performed by aligning ORFs to
235 reference sequences within the PhyloDB database using BLASTX (Cohen et al. 2021), and additional iron oxidation, reduction, storage and acquisition annotations were subsequently assigned using FeGenie (Garber et al. 2020). A small value of 0.03 (approximately the lowest normalized spectral count value in the data set) was added to all counts, thereby removing instances of 0, and allowed for fold change estimates. A permutation test was used to determine differential abundance of proteins between the hydrothermally-influenced sample (n=1) and background sites (n=20) implemented in PANDA-view (Chang et
240 al. 2018). P-values were multiple test corrected using the Benjamini-Hochberg method and the significance cutoff was a false discovery rate (FDR) < 0.1.

3 Results & Discussion

The objective of the Metzyme survey was to track how microbial physiology shifts along natural biogeochemical gradients,
245 with an emphasis here on the tectonically-active tropical southwest Pacific (Beaulieu et al. 2013; Baker et al. 2019). The

section spans multiple biomes, beginning in the oligotrophic tropical North Pacific gyre, latitudinally traversing the nutrient-rich equatorial upwelling zone, and terminating in the oligotrophic South Pacific gyre with a short longitudinal transect off the Samoan Islands, in the vicinity of the NE Lau Basin (Fig. 1).

250   Physiochemical measurements indicated an asymmetry between the tropical northern and southern hemispheres with a difference in thermocline/nutricline depths, oxygen saturation, particle density (turbidity) and salinity (Fig. S2). An oxygen minimum zone (OMZ) resided between 17°N and 3.5°S at 150-1,000m depth, with the OMZ layer directly above excess nitrate+nitrite and phosphate in the northern tropical Pacific (Fig. 1). Equatorial upwelling was evident with nitrate+nitrite and phosphate concentrations reaching 10 µM and 0.5 µM, respectively, in surface waters between 0-3.5°S. Distinct water masses
255   were observed across the section with higher salinity surface water characteristic of the South Equatorial Pacific Intermediate Water present south of the equator, and the North Equatorial Pacific Intermediate Water to the north (Bostock et al. 2010). The South Equatorial Pacific Intermediate Water is associated with a deepening of the thermocline also evident in macronutrient and trace metal nutriclines, with on average <0.15 nM dFe, <0.6 nM dZn, <0.6 nM dCu, <3.1 nM dNi, <80 pM dCd, and <25 pM dCo persisting to 300m in the south Pacific (Fig. 1). Below we report the full-depth trace metal distributions along this
260   natural biogeochemical gradient.

Fig. 1. Trace metal and macronutrient section plots along the Metzyme transect plotted using weighted-gridding interpolation in Ocean Data View. All dissolved metals apart from Co were quantified using seaFAST/ICP-MS, while Co was measured using cathodic stripping voltammetry following UV irradiation. Vertical white lines mark the CTD casts, white dots indicate
265   discrete sampling depths. Six Fe outliers were removed from the section, for full profiles see Fig. 2-4.

Biogeosciences
Discussions
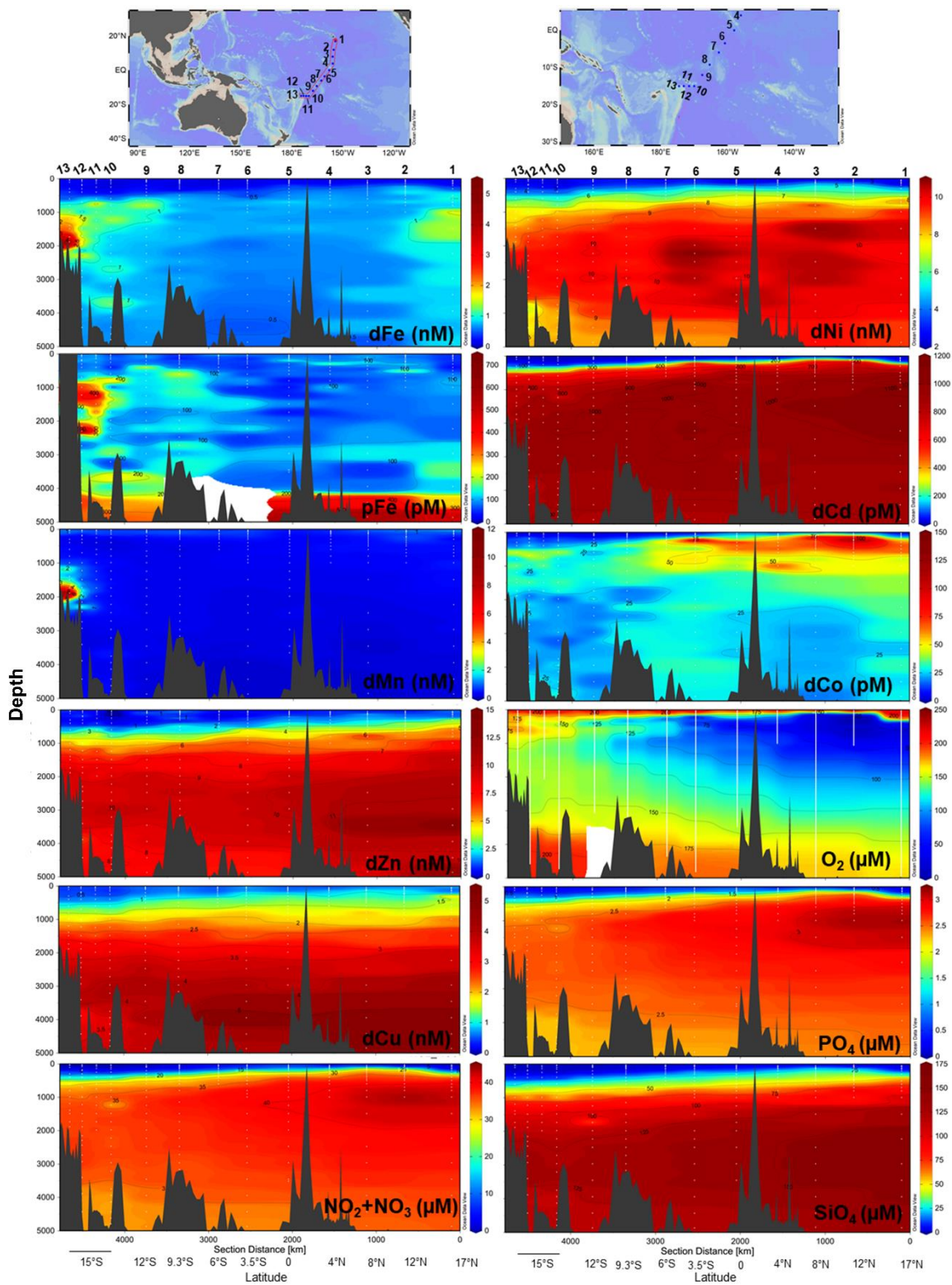
3.1 Biogeochemical controls on dissolved metals in the tropical Pacific (St. 1-8)

Dissolved metal distributions in the upper transect (St. 1-8) reflected regional biogeochemical and physical influences,
270   including biological nutrient utilization in surface waters, redox effects in oxygen minimum zones, heterotrophic
remineralization, hydrothermal input, and deep water scavenging (sorption onto particles, abiotic precipitation, and
biologically-mediated precipitation; Fig. 1). dFe showed a classic hybrid-type profile (Bruland and Lohan 2003), with average
concentrations of 0.15 ± 0.10 nM in surface waters (< 200m) due to biological drawdown, increasing to 0.63 ± 0.30 nM below
the euphotic zone as a result of remineralization (200-3,000m), and stabilizing to an average of 0.65 ± 0.14 nM across the
275   abyssal ocean ($>3,000$ m; Fig. 2). In contrast to dFe, dMn was elevated in surface waters due to dust input and photoreduction
(Sunda et al. 1983; van Hulten et al. 2016), reaching an average 0.80 ± 0.30 nM at 40m, and decreasing to 0.20 ± 0.03 nM by
3,000m. These Mn distributions are typical of the deep Pacific Ocean, with Mn oxidation mediated by Mn-oxidizing bacteria
in aphotic waters (Moffett and Ho 1996; Tebo et al. 2005; van Hulten et al. 2016).

280   A hydrothermal dFe signal was captured off the Hawaiian Island chain at St. 1 (17°N, 154.4°W; Fig. 2), ~212 km away from
the tectonically active Lo'ihi Seamount. Maximum dFe concentrations reached 1.26 nM at 1,000m, consistent with the 1,100
m Lo'ihi injection depth and associated ^{3}He signature (Lupton et al. 2004; Boyle et al. 2005; Wu et al. 2011; Jenkins et al.
2020). Using historical He concentrations and isotope ratio anomalies (δ^3He) from the distal Lo'ihi plume close to our site
(17°S, 152°W; Jenkins et al., 2019a) and converted to excess ^{3}He (Jenkins et al. 2019b, 2020), we calculate a dFe:^{3}He slope
285   ratio of 2.0×10^6. This ratio is in good agreement (to within a factor of 2) with the distal ratio reported by Jenkins et al. (2020)
using multiple distal sites 100-1,000 km from Lo'ihi. Dissolved Mn distributions show only a minor enrichment at this depth,
similar to previous observations (Boyle et al. 2005), and support high dFe:dMn ratios associated with the Lo'ihi hydrothermal
system (Jenkins et al. 2020).

290   **Fig. 2**. Full depth metal profiles for dissolved Fe (red) and Mn (blue), oxygen (black), and primordial ^{3}He used as a signature
of hydrothermal activity (purple). ^{3}He data was previously collected by (Lupton et al. 2004).
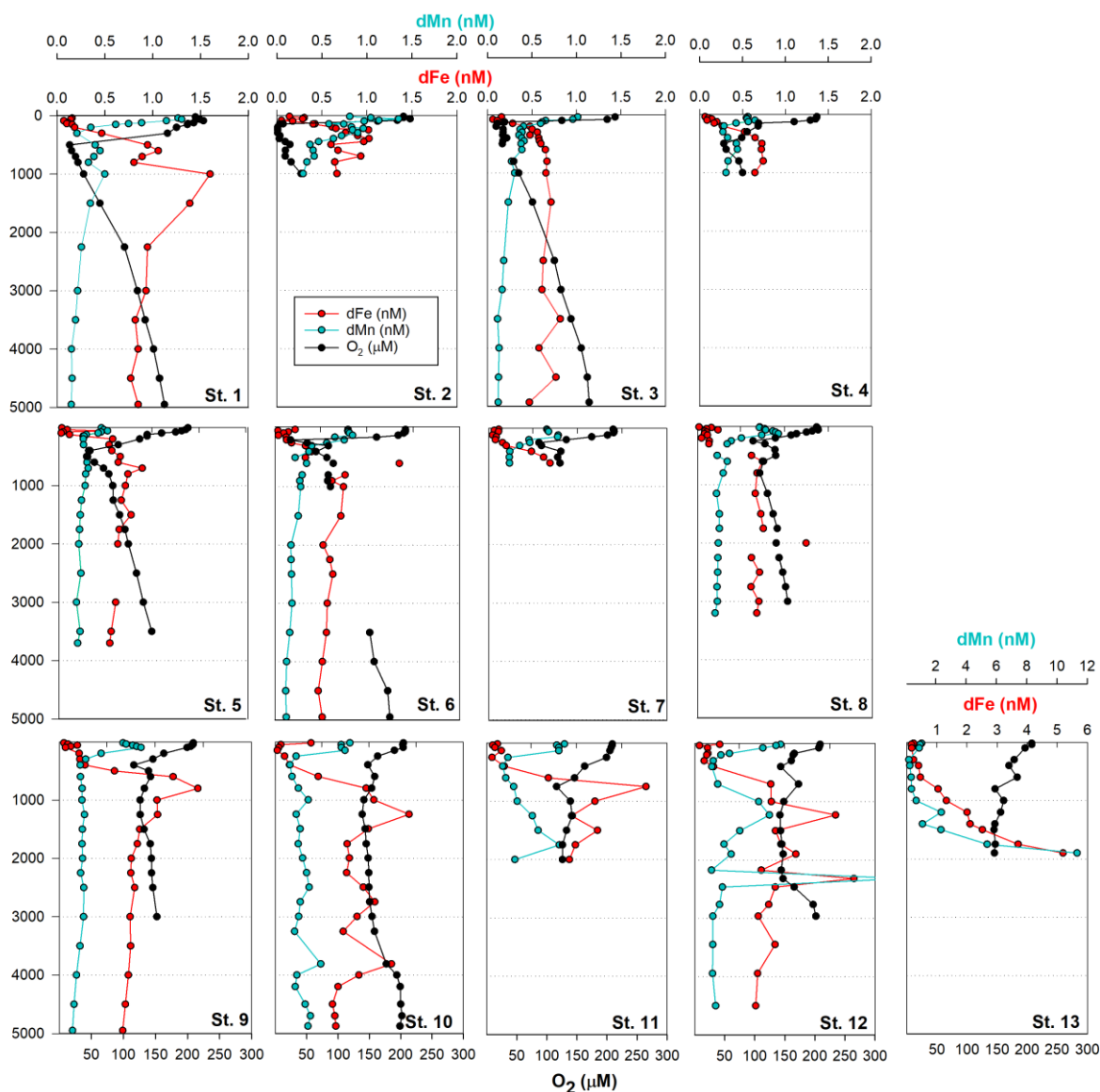
Dissolved Co, like Mn and Fe, reflected a hybrid-type profile with biological uptake in the euphotic zone, remineralization and scavenging influencing its distribution (Fig. 3). In the OMZs located between St. 1-6 (Fig. 1), two dCo plumes were apparent with dCo maxima of 132 pM (St. 2; 1.7 µM O_2) and 116 pM dCo (St. 6; 26 µM O_2) centered at ~200m, as previously discussed for the Metzyme section (Hawco et al. 2020). Dissolved Co is hypothesized to accumulate in the OMZ due to decreased activity of Mn-oxidizing bacteria, which otherwise co-precipitate Co along with Mn oxides onto their cell surface under oxic conditions (Cowen and Bruland 1985; Saito et al. 2017; Hawco et al. 2020).

12

Other bioactive trace metals, including Zn, Cu, Ni and Cd, by contrast followed nutrient-like distributions with biological drawdown resulting in low concentrations in surface waters and accumulation of dissolved metals at depth (Fig. 3-4). Dissolved Zn was on average 1.21 ± 1.42 nM in surface waters of 40 m, and 10.37 ± 0.73 nM by 3,000 m. Dissolved Zn distributions are

305   supported by a strong linear relationship with SiO_4 along the cruise transect, with a Zn:Si slope of 0.069 nmol:µmol and an R^2 of 0.96 (Fig. 3B), which matches the tropical Southeast Pacific value of 0.066 (Roshan et al. 2016). This slope furthermore is close to the 0.053 nmol:µmol ratio used to calibrate Zn:Ca proxies (Marchitto et al. 2000), which is known to deviate depending on ocean basin (Middag et al. 2019). Dissolved Cu was an average of 0.62 ± 0.12 nM in surface waters of 40 m and 4.15 ± 0.19 nM by 3,000m, while dNi showed surface concentrations of 2.54 ± 0.40 nM and 10.25 ± 0.34 nM by 3,000m.

310

Fig. 3 (**a**) Full depth metal profiles for dissolved Co (orange) and Zn (green), oxygen (black), and primordial ^{3}He used as a signature of hydrothermal activity (purple). ^{3}He data was previously collected by (Lupton et al. 2004). (**b**) Dissolved Zn distributions are supported by a strong linear relationship with SiO_4 along the cruise transect, with a Zn:Si slope of 0.069 nmol:µmol and an R^2 of 0.96. This Zn:Si slope is close to the 0.053 nmol:µmol ratio used to calibrate Zn:Ca proxies (Marchitto

315   et al. 2000) (**c**) Zn* Metzyme section, or Zn – 0.053*Si, displaying higher than expected Zn levels in the vicinity of the hydrothermal plume, inferred from Si concentrations.
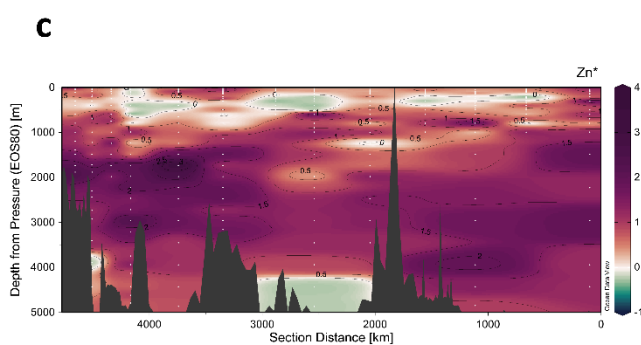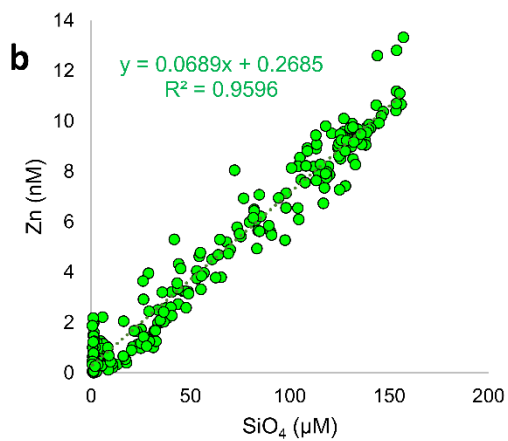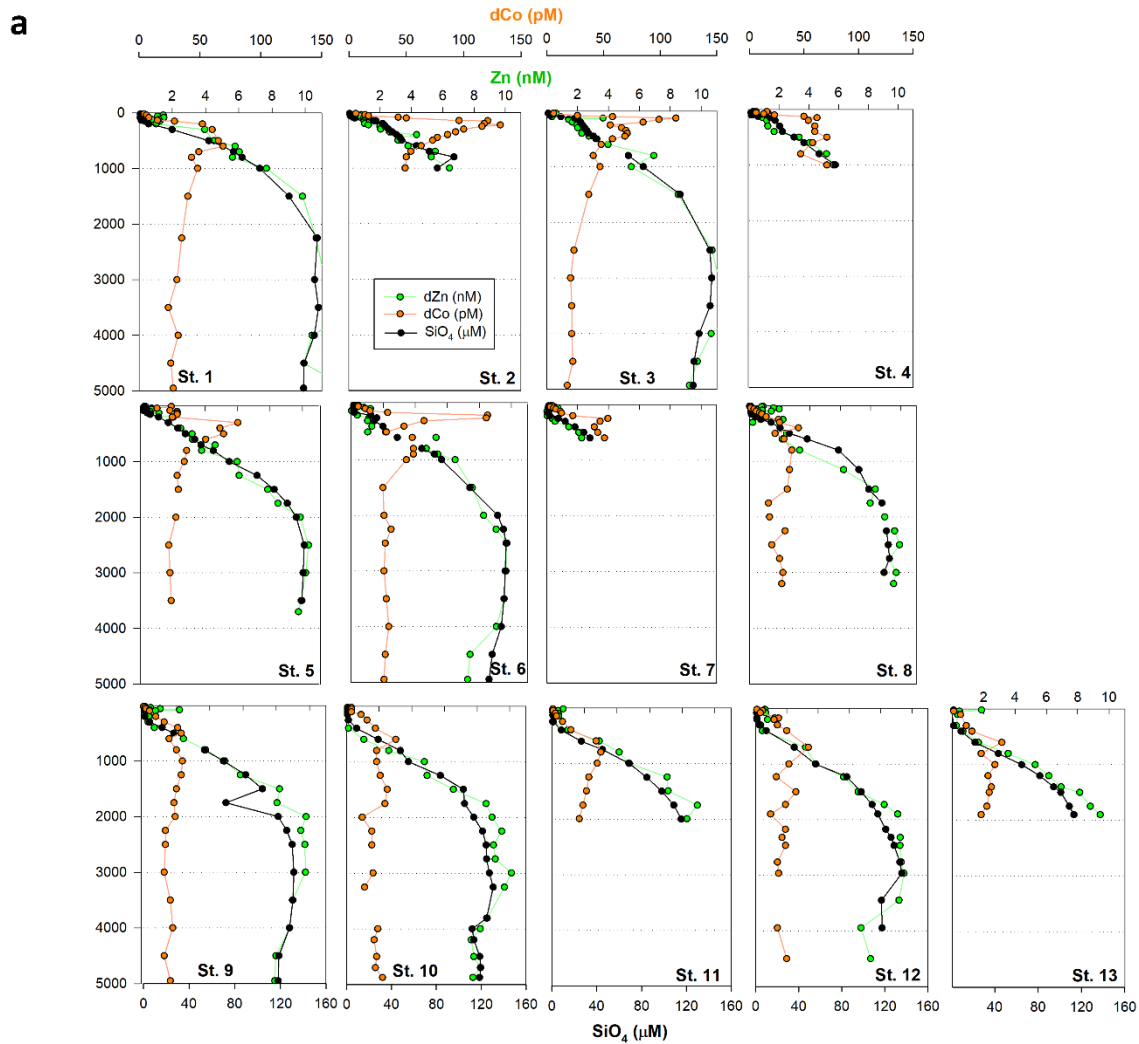
320   In the case of dCd, its stoichiometry (Cd:PO$_4$) varied with depth and between hemispheres, likely due to biological drawdown in surface waters, remineralization at depth, and mixing of water masses. dCd ranged from 3 to 1,129 pM across the section, with an average of 9 ± 6 pM at 40m and 979 ± 40 by bathypelagic depths of 3,000m. Cd showed multiple linear relationships with PO$_4$, where the Cd:PO$_4$ ratio reached 116 pmol:µmol in surface waters <1 µM PO$_4$, and increased to 462 in deep waters containing >1 µM PO$_4$ (Fig. 4B). Our ratios are consistent with reported slopes of 50 in surface waters and 410 in deep waters

325   of the southwest Pacific (Sieber et al. 2019), and 88 in surface waters (<250 m) and 420 in deep waters (>250 m) of the eastern tropical Pacific (Roshan et al. 2017). This large difference in stoichiometry between the shallow and deep, or "kink" in the ratio is observed across the global ocean. In the surface ocean, preferential uptake of Cd relative to PO$_4$ can occur as a result of Fe and/or Zn seawater depletion (Cullen 2006), with Fe-limited cells reducing surface Zn concentrations and continuing to take up Cd through biodilution (Sunda and Huntsman 2000). Fe limitation additionally causes the upregulation nonspecific

330   divalent metal transporters to which Cd competitively binds, further contributing to Cd drawdown from seawater (Cullen 2006; Lane et al. 2008; Saito et al. 2010). Such distinct Cd:PO$_4$ stoichiometries can be transported into larger features, where exported high latitude intermediate waters containing high Cd:PO$_4$ ratios mix with lower latitude water masses containing low Cd:PO$_4$ (Frew and Hunter 1995; Baars et al. 2014; Xie et al. 2015; Middag et al. 2018). In our dataset, Antarctic-sourced seawater is evident by low excess Si, or Si* (Si – NO$_3$), which coincides with the change in slope, and displays a transitional Cd:PO$_4$ ratio

335   (Fig. S3). Lateral differences in stoichiometry across the transect were furthermore demonstrated with a steeper Cd:PO$_4$ ratio of 597 pmol:µmol observed in deep water of the south Pacific (St. 9-13) compared to a slope of 472 pmol:µmol further north (St. 1-8; Fig. 4C). We next contrast these trace metal distributions with hydrothermally-influenced sites in the NE Lau Basin.

Fig. 4 (**a**) Full depth metal profiles for dissolved Cd (navy), Cu (yellow) and Ni (pink). (**b**) Linear relationship between
340   dissolved Cd and PO$_4$ across the transect, separated by shallow, < 1 µM PO$_4$ (red) and deep, > 1 µM (blue). (**c**) Cd and PO$_4$ relationship in the north compared to southwest Pacific. Cd:PO$_4$ relationship for St. 1-8 in deep water (>1 µM) is shown in pink, St. 9-13 (> 1 µM) is shown in brown.
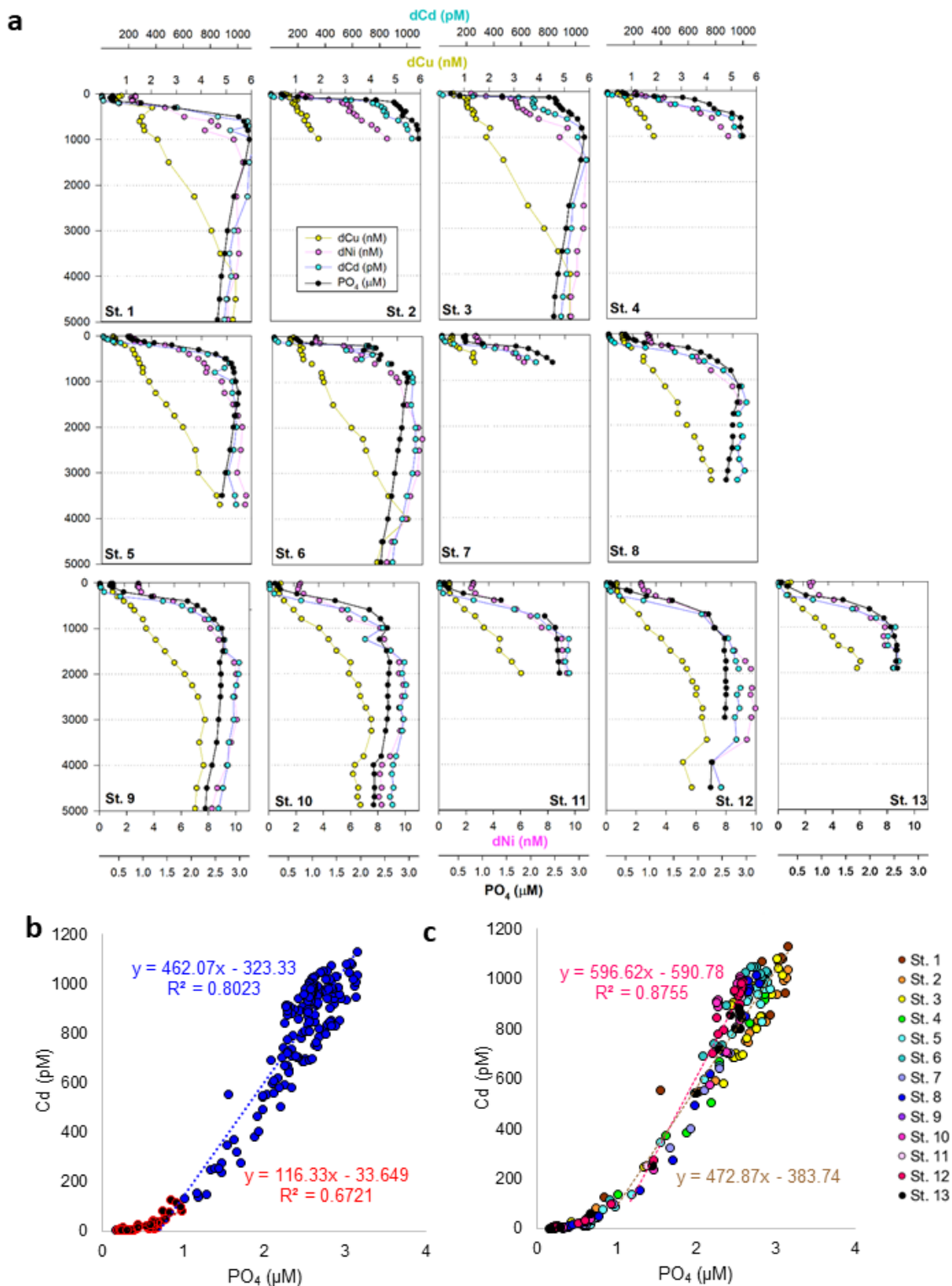
345

3.2 Hydrothermal activity in the southwest Pacific (St. 9-13)

Dissolved metal distributions in the lower transect are consistent with several local hydrothermal sources originating in the NE Lau Basin. δ^3He samples were not collected during the Metzyme expedition, and as a result, comparisons are made using prior δ^3He collected in the region. Most strikingly, a prominent dFe and dMn feature was observed at 15°S and 174.5°W (St.

350   13; Fig. 5A-B). Dissolved Fe and dMn steadily increased to 5.2 and 11.3 nM, respectively, by 1,900 m, in contrast to typical bathypelagic concentrations of ~0.5 nM dFe and ~0.18 nM dMn at stations further north. These maxima were located just 81 km east of a maximum δ^3He (43.4%) centered at 1,726 m, collected at 15°S and 173.1°W two decades prior (Lupton et al. 2004), and could be associated with a common hydrothermal source. Alternatively, an intense δ^3He signal of 58.7% has been measured 168 km west of our site, at 15.64°S and 177.32°W and centered at 1,924 m, and may also be associated with these

355   metal anomalies, although seawater at this depth should advect to the northwest (Fig. S4) (Reid 1997; Lupton et al. 2004; Speer and Thurnherr 2012). Thus, that hydrothermal source is not expected to be responsible for the metal features to the east. No physiochemical signatures were detected using CTD sensors (temperature, salinity, turbidity) implying this was not a near-field hydrothermal plume feature (Fig. S2).

360   The St. 13 dFe/dMn ratio of 0.43 at 1,900m is low compared to the distal plumes from the southern East Pacific Rise and Lo'ihi systems with ratios >2 (Fitzsimmons et al. 2014; Jenkins et al. 2020), likely due to the distinct vent fluid geochemistry, hydrography and underlying geology in this back-arc setting. Hydrothermally-derived Zn was evident with excess Zn (Zn*) in the vicinity, which demonstrated higher than expected Zn concentrations based on its relationship to Si (Zn - 0.053*Si), and similar to observations made in the southern East Pacific Rise (Fig. 3C) (Roshan et al. 2016; John et al. 2018). Other trace

365   metals investigated (Cu, Ni, Co, Cd) did not show distributions consistent with a hydrothermal source (Fig 1).

Fig. 5 (**a**) Total dissolved Fe (red), Mn (aqua) and particulate Fe (brown), Mn (navy) alongside hydrothermal helium (purple) in the NE Lau Basin. Helium data was collected in 1987 and 1990 from identical locations as trace metals in 2011 (St. 10 and 12; Lupton et al. 2004). (**b**) The tropical southwest Pacific leg of the Metzyme transect (St. 9-13) in the Northeast Lau Basin,

370   plotted using GeoMapApp. Hydrothermal vent sites are indicated with green stars (Beaulieu et al. 2013; Baker et al. 2019), and spreading axes are labeled (Martinez et al. 2006; Lupton et al. 2012; Baker et al. 2019). FSC: Futuna Spreading Center; NWLSC: Northwest Lau Spreading Center; RR: Rochambeau Rifts; CLSC: Central Lau Spreading Center; N-ELSC: northern Eastern Lau Spreading Center; FRSC: Fonualei Rift and Spreading Center; MTJ: Mongatolou Triple Junction; NELSC: Northeast Lau Spreading Center. (**c**) Estimated relationship between dissolved iron or manganese and excess helium in the NE

375   Lau Basin. Excess ^{3}He was calculated using δ^3He reported in Lupton et al. (2004) at the same coordinates as Metzyme St. 12, and metal concentrations from Metzyme St. 13. A Type II linear regression is shown for dFe (Glover et al. 2012). dMn showed a nonlinear relationship with excess ^{3}He better fit by an exponential trend line. Note that total He and Ne concentrations were not available and were estimated based on similar δ^3He and depth in the southwest Pacific, using climatological data contained the Global Oceanic Database of Tritium and Helium between 14-17°S and 160-180°W (Jenkins et al. 2019a). Upper water

380   column excess ^{3}He concentrations were extrapolated using historical data from Lupton et al. (2004). (**d**) Dissolved iron profiles at each station plotted with depth (left) and density (right).
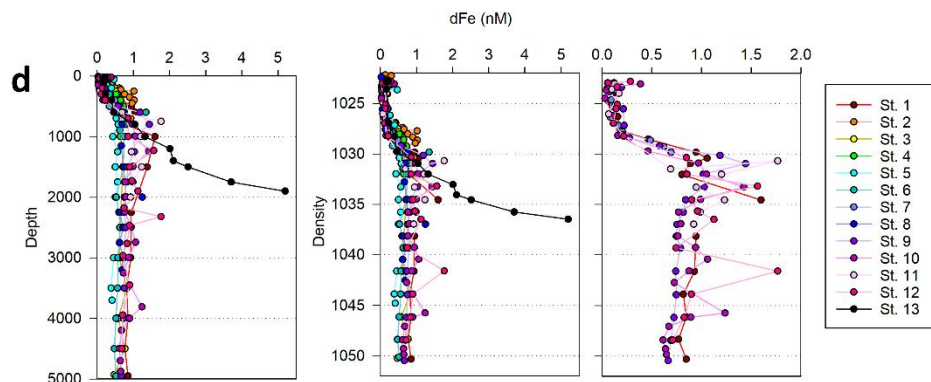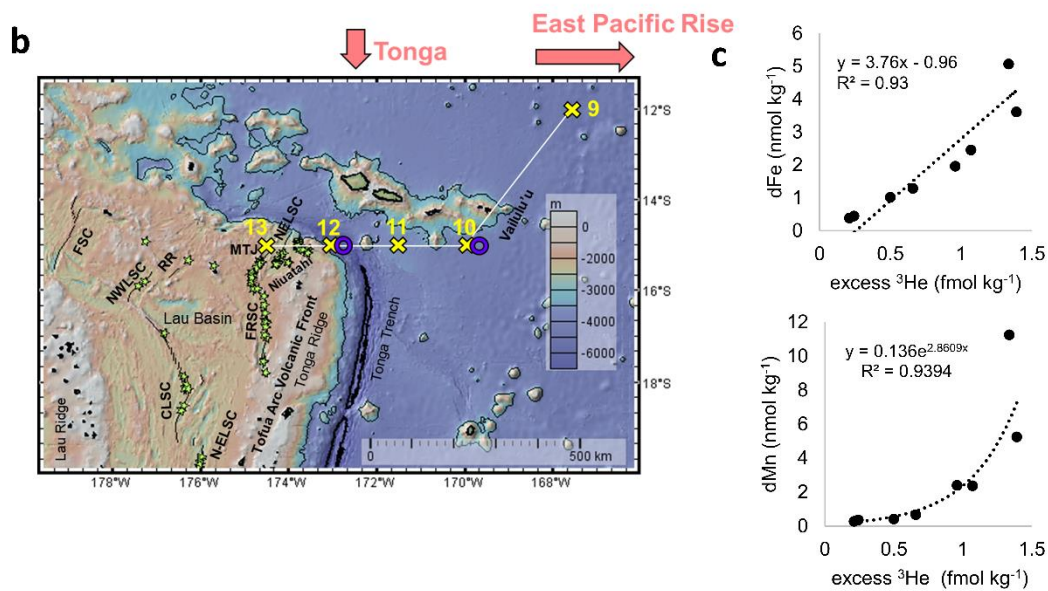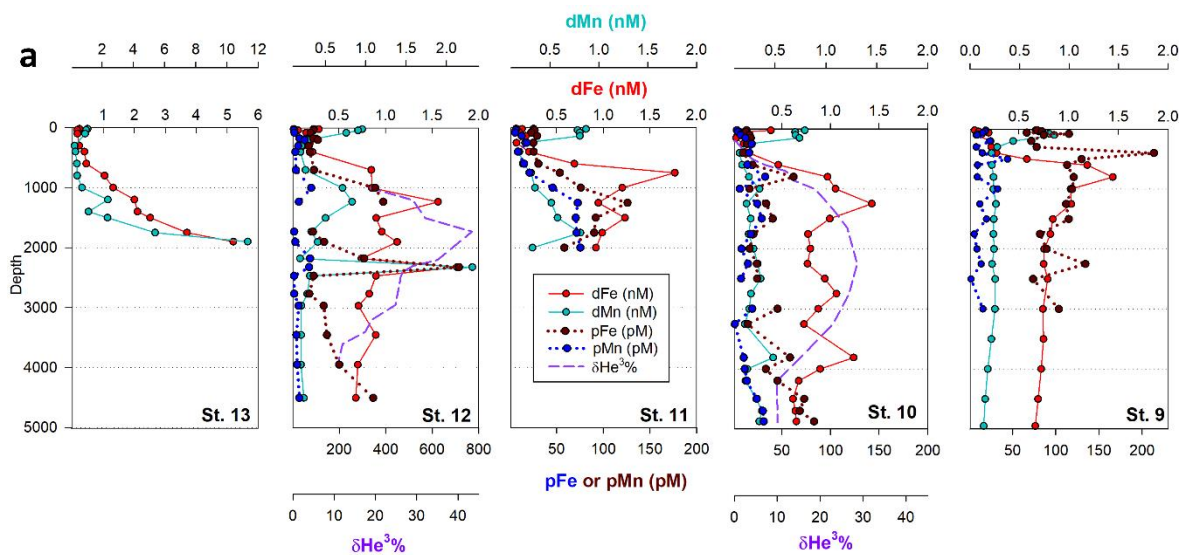
The NE Lau Basin is semi-enclosed, topographically restricted by the Tonga Ridge to the west and south, Lau Ridge to the

385   west, and Zephyr Shoal below 2,000m to the north (Speer and Thurnherr 2012). Distal plumes are therefore expected to vent

to the northwest, consistent with circulation patterns measured from NE Lau Basin float trajectories (Speer and Thurnherr

2012). Elevated dFe and dMn concentrations at St. 13 coincide with where the highest hydrothermal output is expected; north-

bound hydrothermal outflow is steered along the east side of the Tonga Ridge before ultimately escaping into the northwest

(Speer and Thurnherr 2012). This is similar to topographic steering of the Kairei plume along the Central Indian Ridge in the

390   Indian Ocean (Rudnicki and German 2002).

Further east at St. 9-12, dFe and dMn profiles demonstrate additional hydrothermal sources showing lateral consistency ~300

km apart (Fig. 5A). As seawater at 2,000 m advects in a northwestern direction (Reid 1997; Lupton et al. 2004), it is unlikely

the sharp feature detected at St. 13 was contributing to elevated metal concentrations at these stations further east (St. 9-12).

395   They additionally reside in different density layers (Fig. 5D). Seawater samples collected during the Metzyme expedition from

the identical location as the previously measured ^{3}He core (δ ^{3}He = 43.3%; Lupton et al. 2004) show two dFe and dMn peaks

straddling the δ^3He maximum at 1,726 m with a concave distribution (Metzyme St. 12). The shallower metal peaks occurred

at 1,230 m, with 1.6 nM dFe and 0.83 nM dMn, while the deeper peak consisted of 1.8 nM dFe and 2.3 nM dMn at 2,320m

(Fig 5B). These shallow and deep dFe and dMn signals are also present 333 km east of the Tonga Ridge at 15°S and 170°W

400   (St. 10), where dFe and dMn were 1.4 and 0.22 nM, respectively, at 1,243 m depth, and 1.1 and 0.26 nM, respectively, at 2,744

m (Fig. 5B). Although the St. 12 deep dFe signal is much sharper than the one at St. 10, the integrated areas of both peaks

between 2,000 – 3,000 m are comparable (907 vs. 849 µmol/m^2, respectively) suggesting a similar iron supply, and they fall

in the same density layer (Fig. 5D). Notably, particulate Fe matches the dual dFe peaks and therefore supports two separate

hydrothermal sources at St. 10 and St. 12, and demonstrates that particle formation and scavenging is not driving the concave

405   dissolved Fe profile distributions. A third peak is present at St. 10 at 3,803 m where dFe reaches 1.24 nM and dMn 0.48 nM,

and at St. 12 at 3,450 m where dFe reaches 0.9 nM, although the Lau Basin sea floor is not that deep and neither signal could

originate from there. A shallow dFe signal was furthermore captured at St. 11 where only a partial profile was obtained from

the upper water column. Apart from multiple hydrothermal sources, sills may also explain the multi-featured metal profiles

with seawater advecting away from the hydrothermal source(s) coming into contact with sill structures, disrupting flow and

410   dispersing the plume in three dimensions (Fig. 1). Elevated subsurface dFe was evident as far north as St. 9 (12°S, 167.6°W)

where dFe reached 1.4 nM at 800m (Fig. 2).

As St. 9 is our most northern station that captures hydrothermal influence in the dissolved metal fraction, we suspect the plumes

captured in this survey do not continue north, and instead discharge laterally or to the northwest where they escape to the

415   tropical southwest Pacific. There was little evidence of the East Pacific Rise plume-derived dFe advecting west over ~6,000

km in the St. 10 dFe profiles (Fig. 2A), despite the pronounced δ^3He of 30% observed at 2,500 m at this location (Lupton et

al. 2004) and a dFe:^{3}He signal evident just ~550 km south of this site (Fitzsimmons et al. 2014). It is possible the St. 10 dFe peak at 2,750 m is associated with the East Pacific Rise, but likely that any East Pacific Rise-sourced Fe is overshadowed by the more intense local plumes at St. 12.

420

Our trace metal profiles are consistent with the presence of multiple, diverse sources of venting in this region of the NE Lau Basin (Baker et al. 2019), and exhibit changes in non-buoyant plume location, intensity, and/or depth in the water column compared to the ^{3}He anomalies that were more than two decades earlier, in 1987 (Lupton et al. 2004). The core of the ^{3}He plume identified by Lupton et al. (2004) is located at the same site as our St. 12, approximately 81 km east of where the

425 strongest dFe and dMn signal was detected at our St. 13 (Fig. 5B). Furthermore in the original ^{3}He data set, there was no signal associated with shallow dFe and dMn enrichments at ~1,200m, where only the deeper δ^3He signature centered at 1,726 m was apparent (Lupton et al. 2004). We hypothesize that these differences within the dynamic NE Lau Basin system may be due to changes in hydrography in the pathways and/or flux of the plume materials exiting the Lau Basin together with recognition that extensive new eruptions should be expected to have arisen along his fast spreading back-arc system (up to 42 mm/year

430 full spreading rate; Baker et al., 2019) since the corresponding ^{3}He sampling was conducted in 1987. Multiple distinct hydrothermal vent sources appear responsible for the metal-rich plumes observed at different depths/density surfaces observed here, all of which should be expected to contribute to the larger excess ^{3}He pool (Fig. 5A) (Lupton et al. 2004; German et al. 2006).

435 The Northeast Lau Basin contains 135 active hydrothermal sites with new sites continuing to be discovered (Beaulieu et al. 2013; Baker et al. 2019). The exact vent sources responsible for the dFe and dMn distributions observed here are unknown. The strongest metal plume signals in this study come from St. 13, which is <50 km from the NE Lau Basin Spreading Center (NELSC) and the Mangatolo Triple Junction (MTJ) which have plume depths between 1,300-2,400m (Fig. 5B) (Lupton et al. 2004; Kim et al. 2009; Baker et al. 2019). There is extensive arc volcanism to the east which likely generates further complexity

440 with additional vents feeding multiple shallower plume depths (Staudigel et al. 2004, 2006; Baker et al. 2019). This is observed in dFe and dMn profiles from St. 12 eastward when compared to the broad coalesced plume that dominates ^{3}He distributions in the NE Lau Basin (Lupton et al. 2004). Although active hydrothermal venting has been measured East of the Tonga Arc at the Vailulu'u Seamount Somoan Island chain hotspot (Staudigel et al. 2004), this system is not likely responsible for the intense ^{3}He plume given that the maximum ^{3}He signal is located within the W-E lateral bounds of the Lau Basin (Lupton et

445 al. 2004), and that the St. 13 metal plume falls along the ridge axis (Fig. 5B). The Vailulu'u Seamount additionally has a crater depth of just 750 m (Staudigel et al. 2004), which is too shallow to explain the strong metal-enriched feature we report here at 1,900m.

Using metal concentrations from St. 13 and δ^3He quantified by Lupton et al. (2004) from our St. 12, we estimate the maximum

450 amount of dFe relative to excess ^{3}He released from this back-arc setting (Fig. 5C; Table 3). (For comparison, the relationship

between St. 12 dFe and ^{3}He is shown in Supplemental Fig. 5.) St. 13 dFe showed a linear relationship with ^{3}He with a slope of 3.8 x 10^6 while dMn, in contrast, behaved non-conservatively. Geostrophic flow supports northwest circulation at this depth (Reid 1997; Lupton et al. 2004; Speer and Thurnherr 2012), and dFe:^{3}He ratios of 3.8 x 10^6 represent a significant source of Fe being introduced to microbial communities at bathypelagic depths in this direction. The dFe:^{3}He estimates for this back-

455   arc area (Table 3) are distinct from, but comparable to, what has previously been reported for other major plumes at a Mid Ocean Ridge (southern East Pacific Rise) and an intra-plate hotspot (Lo'ihi Seamount) (Fitzsimmons et al. 2017; Jenkins et al. 2020). Our metal data demonstrates that the hydrothermal plume observed by Lupton et al. (2004) has the capacity to export large amounts of Fe and Mn to the ocean interior, similar to the southern EPR and Lo'ihi systems (Resing et al. 2015; Jenkins et al. 2020). We next discuss how microbial physiology may have been impacted by this distal plume.

460

Table 3. Dissolved metal to excess ^{3}He ratios among the NE Lau Basin, Lo'ihi Seamount, and southern East Pacific Rise distal plumes. The NE Lau Basin ratio was calculated here using reported and extrapolated δ^3He in Lupton et al. (2004) from the same location as Metzyme St. 12, and using Metzyme St. 13 dissolved metal concentrations. Excess ^{3}He was determined following the equation in Jenkins et al., (2020). The Type II linear regression slope is shown for dFe. St. 13 dMn showed a

465   nonlinear relationship with excess ^{3}He better fit by an exponential trend line. Note that He and Ne concentrations were not available from Lupton et al. 2004 and were instead estimated based on similar δ^3He values and depths in the Global Oceanic Database of Tritium and Helium (Jenkins et al. 2019a) between 14-17°S and 160-180°W. Helium isotope solubility fractionation factors, He and Ne solubilities, and Type II regressions were calculated using *healph*, *LJSolMol*, and *lsqfitma* Matlab functions (Jenkins et al. 2019a; b, 2020).

	NE Lau Basin (this study)	Lo'ihi Seamount (Jenkins et al. 2020)	East Pacific Rise (Fitzsimmons et al. 2017)
dFe:^{3}He	3.8 x 10^6	4.4 x 10^6	4.3 x 10^6
dMn:^{3}He	$0.14e^{(2.86x)}$	1.0 x 10^6	2.3 x 10^6

470

3.3 Microbial community composition in background and hydrothermally-influenced seawater

The influence of distal hydrothermal plume geochemistry on surrounding microbial physiology and ecology was assessed using comparative metaproteomics with the 3-51 µm fraction of the Metzyme meta-'omic data set (Cohen et al. 2021). Since hydrothermal vents were not the focus of this expedition, real-time instrumentation for tracking hydrothermal signatures was

475   not onboard the ship. Instead, seawater samples and biomass was collected at the same location where hydrothermal activity had been observed previously, at St. 12 (Lupton et al. 2004), and analyzed back in the laboratory. We therefore were unaware that the largest metal signatures were at St. 13, or that present-day plume maxima at St. 12 were at 1,200 and 2,200 m, and so biomass was not collected at these depths. However, biomass *was* obtained in the vicinity of hydrothermal influence, at St. 12 (15°S, 173.1°W) at 1,900m, where dissolved and particulate metals were higher than background concentrations. Other deep

480   (≥ 200 m) samples collected across the transect served as background, non-hydrothermally-influenced vent sites (*n*=20).

Biogeosciences
Discussions
EGU Open Access

Metzyme metaproteomes from the upper water column are used comparatively to the deep ocean, but are not the focus of this analysis.

485   Microbial communities collected on the 3-51 µm filters were composed of archaea, heterotrophic bacteria, viruses, cyanobacteria, protists, and metazoans (Fig. 6). In particular, dinoflagellates, Alphaproteobacteria and *Prochloroccocus* accounted for an average of $50 \pm 9\%$ (± 1 standard deviation) across all of the sample communities based on NSAF-normalized proteins (Fig. 6). The presence of prokaryotic organisms smaller than 3 µm represents particle-associated assemblages, filamentous chains, host-symbiont relationships, or cells aggregated or adsorbed onto biomass-dense filters. Samples collected

490   from the upper water column (< 200m) showed higher proportions of cyanobacteria while relative distributions of the other abundant groups, including Gammaproteobacteria and Alphaproteobacteria, were more abundant with depth (Cohen et al. 2021). Although the 0.2-3 µm fraction would certainly contain pelagic bacteria and archaea sensitive to hydrothermally derived chemical species, we were not able to extract enough biomass from this filter fraction for the metaproteomic analysis.

495   Amplicon sequencing of ribosomal RNA was used to determine community composition along the Metzyme transect (Cohen et al. 2021). A PCoA analysis constructed with 18S and 16S rRNA operational taxonomic units (OTUs) demonstrated that the eukaryotic and prokaryotic communities at the hydrothermal site largely resembled that of background locations (Fig. S5). These similarities between the distal plume-influenced and background prokaryotic communities agree with findings from buoyant hydrothermal plumes at vent-sites along the Eastern Lau Spreading Center (ELSC) where it has been argued that

500   microbes sourced from background seawater are entrained into and displace seafloor organisms (Sheik et al. 2015). Deep sea communities therefore may be relying on metabolic plasticity to exploit a variety of environmental conditions, enabling the occupation of both hydrothermal and non-hydrothermal influenced seawater systems. Protistan groups such as ciliates, stramenopiles, dinoflagellates and radiolarians are also ubiquitous in the deep ocean, and may serve as important vectors for transferring carbon obtained from vent sites to the broader bathypelagic ocean (Olsen et al. 2015; Murdock and Juniper 2019;

505   Mars Brisbin et al. 2020). However, hydrothermal populations can be genomically distinct from background communities at a fine taxonomic level, which has been observed in vent-influenced protistan communities using amplicon sequence variants (ASVs) (Mars Brisbin et al. 2020; Hu et al. 2021) and bacterial functional genes (Mino et al. 2013, 2017), although this was not observed here using an OTU approach. Interestingly, disconnects between the amplicon and proteomic datasets were apparent with the 16S rRNA analysis indicating cyanobacteria were one of the most relatively abundant taxa identified even

510   in deep waters ($\geq$ 200 m; Fig. S6), while <25% of deep prokaryotic proteins belonged to cyanobacteria (Fig. 6). Such differences could be due to extraction, primer, and/or sequencing bias (VerBerkmoes et al. 2009; Brooks et al. 2015), limited references in taxonomic databases (Orellana et al. 2019), or biological differences in cellular pools of RNA and proteins. Regardless, both analyses indicate that at a coarse taxonomic level, particle-associated prokaryotic and microeukaryotic communities in this size fraction at the hydrothermal site were similar to those of background seawater.

22

515

3.4 Metaproteomics of particle-associated microbial communities in hydrothermally-influenced seawater

Metaproteomics was performed by injecting purified peptides from each station and depth onto an HPLC system in 2-dimension active modulation mode coupled to an orbitrap mass spectrometer (LC/MS/MS) running in data dependent acquisition (DDA) mode (see methods) (McIlvin et al. in prep). The full dataset contains 9,796 proteins, 99,143 peptides and

520   366,025 total spectral counts, of which 80% of the proteins have a taxonomic and/or functional annotation (Cohen et al. 2021). To investigate metabolically active proteins influenced by hydrothermal metal release, a permutation test was performed with only deep samples (≥ 200 m, n = 21) comparing background non-hydrothermally influenced vent sites (n = 20) to a single site within the vicinity of a hydrothermal plume (St. 12, 1,900m). A two-tailed asymptotic general independence test was used followed by Benjamini-Hochberg p-value correction (FDR < 0.1). Of the 3,492 deep (≥ 200 m) proteins, 201 were either more

525   abundant at the hydrothermal site compared to background sites, or solely identified at the hydrothermally-influenced site (FDR < 0.1; Table S2). Consistent with the amplicon sequencing analysis, the taxonomic identity of hydrothermal plume-associated proteins largely resembled that of background sites. Eighty-four percent of these hydrothermally-influenced proteins belonged to the particle-associated prokaryotes; of the 201 proteins enriched at the HT site, 169 were prokaryotic, 28 eukaryotic, and 4 viral (*Prochlorococcus* phage P-SSM2 and P-SSP7; *Synechococcus* phage S-RSM4; Fig. 6). The implications

530   of hydrothermal activity on microbial metabolism was next explored by examining differentially abundant proteins involved in metal transport, amino acid metabolism, and chemoautotrophy.

Fig. 6. Whole community phyla and supergroup-level relative community abundance determined through metaproteomics on the 3-51 µm size fraction, modified from Cohen et al. 2021 (Left). Only peptide spectral counts matching open reading frames

535   (ORFs) with a classified taxonomic annotation and lineage probability index greater than 0.7 are shown. Exclusive spectral counts were normalized following the NSAF (normalized spectral abundance factor) approach. Differential abundance of proteins in the hydrothermal plume (St. 12, 1,900m) compared to non-HT, background deep sites (n=20) (Right). The x-axis represents protein abundance (NSAF-normalized spectral counts), and y-axis is the $\log_2$ fold change in protein abundance between the HT site (St. 12, 1,900m) and the average of deep (≥ 200 m) background sites (n = 20). The horizontal purple lines

540   mark a $\log_2$ fold change of 2 or -2, for a 4-fold increase or decrease in protein abundance, respectively. A small value of 0.03 was added to normalized spectral counts to allow for log transformation. Linear arm contains proteins not identified in the hydrothermal plume. Note not all protein groups of interest are annotated; for a complete list of key proteins identified see Fig. 4 and Table S2. (Nxr: nitrate oxioreductase; SoxF: sulfur oxidation protein; Amo: ammonia monooxygenase; PS I: photosystem I reaction center protein).
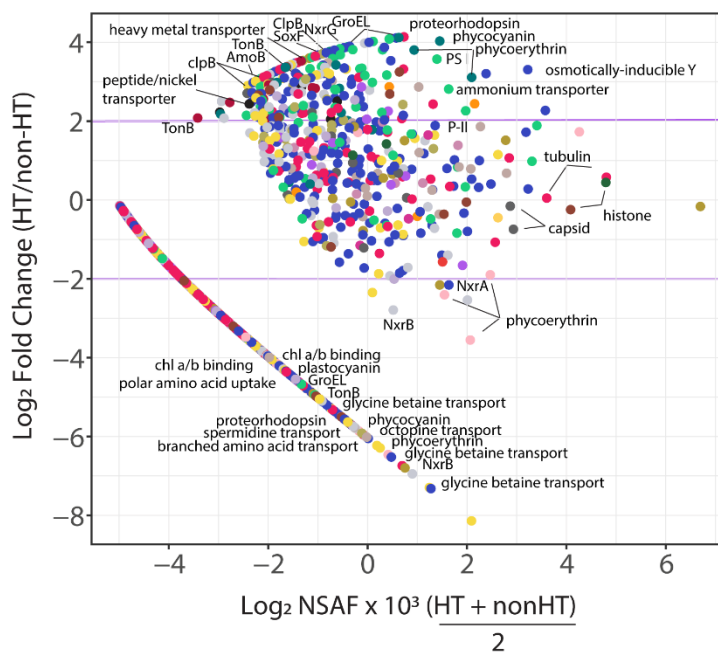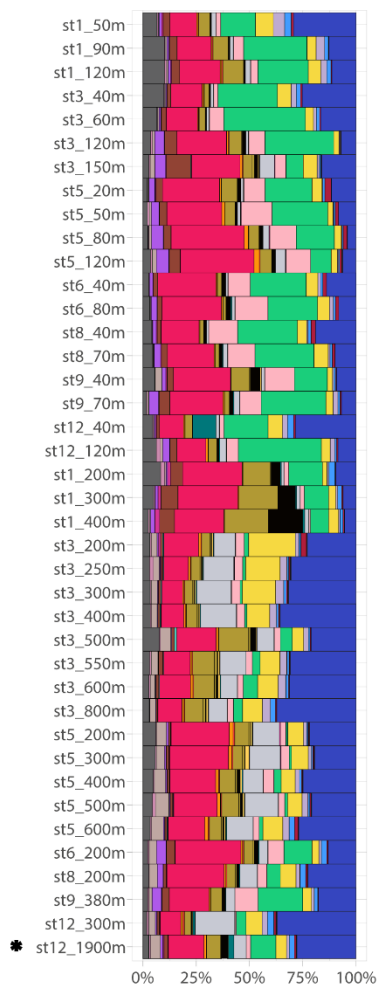
545

3.5 Microbial trace metal and organic transporters, structural proteins and proteases potentially utilized in the dispersing plume

A number of transporters identified may aid in uptake and efflux of metals and organics originating from the hydrothermal
550   plume. These include a heavy metal transporter protein belonging to the Betaproteobacteria *Burkholderiales* family which was
not detected outside plume-influenced seawater (FDR = 3×10^{-4}; Fig. 6). Although trace metals are micronutrients required by
cells to carry out essential biochemical reactions, high concentrations lead to oxidative stress and cell damage. Therefore, this
protein may be useful, either for uptake or efflux out of the cell. Bacterial TonB outer membrane receptor proteins were
investigated as they are involved in transport of siderophores, inorganic metals, vitamin B_{12} and carbohydrates (Noinaj et al.
555   2010). The majority of TonB proteins identified were not differentially abundant (n = 83, Fig. 7), although 3 in particular were
enriched in the vicinity of the plume. Two of these TonB proteins were 4-fold (FDR = 3×10^{-4}) and 6-fold (FDR =0.006) more
abundant in the plume and belonged to the *Flavobacteriales* family within Bacteroidetes. One contained the SusC and CirA

domains characteristic of carbohydrate and inorganic Fe uptake, respectively, and the other contained the SusC, B_{12} (BtuB) and FepA siderophore domains. An additional TonB protein was 9-fold more abundant in the hydrothermal plume (FDR =

560 0.006), belonging to the *Alteromonadales* family within Gammaproteobacteria, and containing the BtuB domain. Two of 9 putative ABC transport system siderophore transporters belonging to *Rhizobiales* Alphaproteobacteria and *Vibrionales* Gammaproteobacteria were additionally enriched in the plume-influenced seawater (FDR = $3x10^{-4}$ and $9.7x10^{-4}$, respectively). Elevated siderophore transporters may be consistent with increased ligand production in plumes, as has been invoked in stabilizing hydrothermal Fe through organic complexation (Bennett et al. 2008). Although TonB genes are highly expressed

565 in Gammaproteobacteria from the Guaymas Basin hydrothermal plume (Li et al. 2014), we did not find evidence for overall enrichment with only these 3 out of 83 TonB transporter proteins identified as differentially abundant in the plume, suggesting these transporters are broadly utilized by deep sea bacterial communities. The three that are specific to the hydrothermal plume may belong to bacterial strains that were relatively more abundant in the plume environment, or that contain protein isoforms with distinct functional roles.

570

Similar to the TonB transporters, NikA nickel/metallophore ABC transporters, used for the uptake of metals or oligopeptides, are ubiquitous in the deep ocean (Fig. 7). Three proteins however were differentially abundant in the plume; two belonged to *Rhizobiales* Alphaprotebacteria and one to *Thermoplasmatales* archaea, and were 10-fold (FDR = $3x10^{-4}$), 9-fold (FDR=0.01), and 5-fold (FDR=0.01) more abundant in the plume, respectively. The Nik ABC transport system may import Co as well as

575 Ni (Rodionov et al. 2006), and it is unknown whether Mn may also be imported through this uptake system, or whether high concentrations of hydrothermal Mn could competitively inhibit Ni/Co uptake. Finally, a sodium/solute family symporter specific to acetate and belonging to SAR 11 Alphaproteobacteria was 8-fold more abundant at the hydrothermal site (FDR = $3x10^{-4}$), with this family of transporters also enriched in transcripts at Guymas Basin (Dick et al. 2013). This collection of transport proteins reflects potential mechanisms for importing or exporting metals and organic resources sourced from the NE

580 Lau Basin distal hydrothermal plume.

Protein folding components and proteases were elevated in the plume and suggest a concerted effort to maintain cellular structure and utilize organic nitrogen. Twenty-one of 115 globally detected GroEL chaperone proteins involved in protein folding were relatively abundant at 1,900m (FDR < 0.1), belonging to *Rhodobacterales*, *Rhizobiales* and PS1 clade members

585 of the Alphaproteobacteria, *Legionellales* Gammaprotebacteria, Poribacteria, Planctomycetes, Chloroflexi, and cyanobacteria (Fig. 7). Microbes residing in hydrothermal systems are acclimated to extreme temperature and pressure (Merino et al. 2019), and chaperone GroEL proteins are hypothesized to be advantageous to thermophilic hydrothermal vent bacteria requiring a structural defense against the high temperature environment which can lead to protein misfolding (Wei and Zhang 2010; Chen et al. 2013). As this was a distal hydrothermal plume at ambient temperature, the identification of these proteins may represent

590 residual proteins from microbial communities that were transported from near-field vent sites during plume mixing and seawater entrainment. In addition, 4 of 8 Clp proteases were solely detected in plume-influenced seawater, belonging to

Altermonadales and *Virbionales* Gammaproteobacteria and Chloroflexi (FDR = $3\text{x}10^{-4}$). Clp proteases are multi-subunit ATP-dependent proteins that are found in diverse microorganisms including hyperthermophilic bacteria (Ward et al. 2002). Hydrothermal vents support dense chemosynthetic populations producing organics that may be accessed by heterotrophs using

595 such proteases (Bennett et al. 2013; Dick 2019). These proteases were not present at surveyed OMZs across the transect, and Clp protease gene expression was similarly uniquely elevated at the Guaymas Basin hydrothermal vent and not in the Eastern Tropical South Pacific (ETSP) OMZ (Dick et al. 2013). This protease therefore may be specific to hydrothermal plume-associated heterotrophs.

600 Amino acids in particular can be stabilized in reducing, metal-rich and acidic vent environments (Fuchida et al. 2014), and hence, they may also be entrained into dispersing hydrothermal plumes. Certain amino acid transporters were relatively abundant in the plume-influenced seawater and may play a role in directly importing labile amino acids from the plume, including 4 branched and 1 L-amino acid transporters belonging to members of Alphaproteobacteria and Gammaproteobacteria (FDR ≤ 0.03). Heterotrophic plume microbes therefore appear to reinforce cellular structure using chaperone proteins, import

605 amino acids, and express peptidases to potentially take advantage of available organic material.

3.6 Chemoautotrophy & remnant phototrophic metabolism in hydrothermally-influenced deep seawater

Chemoautotrophic metabolism was detected in the plume with ammonium, nitrite and sulfur oxidation proteins present. Many of these proteins were also present at OMZ sites and elsewhere along the transect, supporting widespread chemoautotrophy in the deep ocean (Fig. 7). One of three ammonia monooxygenase proteins (AmoB) belonging to *Thaumarchaeota* was 6-fold

610 more abundant in the plume (FDR = 0.07; Fig. 6). These transcripts are similarly elevated in hydrothermal systems (Baker et al. 2012) and genes are present in metagenome-assembled-genomes of the Eastern Lau Basin (Anantharaman et al. 2016). *Thaumarchaeota* is known to carry out ammonia oxidation in this region of the central Pacific (Santoro et al. 2017), and this process is not unique to hydrothermal plumes. One of 31 detected nitrite oxidoreductases, predicted to bind molybdenum and responsible for the conversion of NO_2 to NO_3 (NxrG), was attributed to the *Brocadiales* family within Planctomycetes and

615 was relatively abundant in the plume and detected only at this location (FDR = $3\text{x}10^{-4}$). These distributions support nitrification as a ubiquitous chemoautotrophic strategy (Pachiadaki et al. 2017; Saito et al. 2020), although chemoautotrophs likely have a competitive advantage over heterotrophs in low organic, reducing environments with elevated ammonium and nitrite that can be oxidized as energy sources (Dick et al. 2013). Sulfur oxidation was potentially occurring, with SoxF belonging to *Rhodobacterales* Alphaproteobacteria only detected in the plume-influenced seawater (FDR = $3\text{x}10^{-4}$). However, this SoxF

620 protein was also present in surface waters (< 200m) throughout the central Pacific transect, and may also be utilized by heterotrophic bacteria residing in oxygenated waters performing anaplerotic inorganic carbon fixation via sulfur oxidation (Muthusamy et al. 2014). Other sulfur oxidation proteins known to be relatively abundant in hydrothermal plume metatranscriptome were not detected (SoxA, DsrA) (Dick et al. 2013; Anantharaman et al. 2016). Metals and sulfide derived from vent fluid likely formed inorganic metal-sulfide clusters, reducing metal toxicity in the microbial community (Edgcomb

625 et al. 2004) and limiting the bioavailability of H_2S to sulfide oxidizing organisms (Hsu-Kim et al. 2008; Sheik et al. 2015). Lastly, heterotrophic Mn-oxidizing bacteria are a major conduit for Mn oxide precipitation in non-buoyant plumes (Cowen et al. 1990). Lithotrophic Mn oxidation is also theorized to occur in Mn(II)-rich vent fluids (Templeton et al. 2005) although the taxonomic groups carrying out this process remain unknown. Multicopper oxidase enzymes responsible for Mn oxidation in cultured hydrothermal bacteria (Dick et al. 2006) were not detected in the plume-influenced sample. It is possible that

630 environmental Mn oxidation proteins differ from those characterized in our reference databases, and are therefore missed during bioinformatic annotations.

The majority of photosynthetic proteins detected were highly represented in surface waters, and included the pigments phycoerythrin, phycocyanin and chlorophyll *a* binding proteins, and photosynthetic carbon fixation components flavodoxin

635 and carbon concentrating proteins. Unexpectedly, a portion of differentially abundant proteins in the hydrothermally-influenced seawater (at 1,900 m) compared to background deep sites belonged to *Prochlorococcus* (20%), and several light-associated proteins were differentially abundant, including phycoerthyrin, phycocyanin, photosystem I subunit XI, chlorophyll a/b binding proteins, proteorhodopsin and Rubisco (Fig. 6). The abundance of these proteins may represent metabolically active phototrophic cells maintaining core metabolism while rapidly sinking to the deep ocean attached to larger particles in

640 the 3-51 μm size range, similar to fast-sinking, healthy diatom cells being detected at 4,000m in the Indian, Atlantic and Pacific Oceans (Agusti et al. 2015). It is unclear if these cells are photosynthetically viable, or partially degraded, and the abundance of these proteins at depth should be investigated in future studies. Photosynthetic green sulfur bacteria have been isolated from a deep sea hydrothermal vent in the East Pacific Rise, and it has been argued these organisms use geothermal radiation as a light source (White et al. 2002; Beatty et al. 2005). The possibility of geothermal light biochemically stimulating

645 photosynthetic proteins from sinking cyanobacterial cells warrants further exploration.

Fig. 7. Heatmap displaying relative protein abundance for all proteins detected involved in chemoautotrophy, protein degradation, protein folding, and resource transport. Each row represents a unique protein with associated normalized spectral counts. Gray represents no protein detection. The sample collected in from the hydrothermal plume (HT; St. 12, 1,900 m) is

650 shown alongside other deep samples (≥ 200 m) collected along the Metzyme transect, including those within the OMZ region (St. 1-6, ~150-1,000 m). See Table S2 for the full list of proteins and annotations.

Biogeosciences

Discussions

EGU
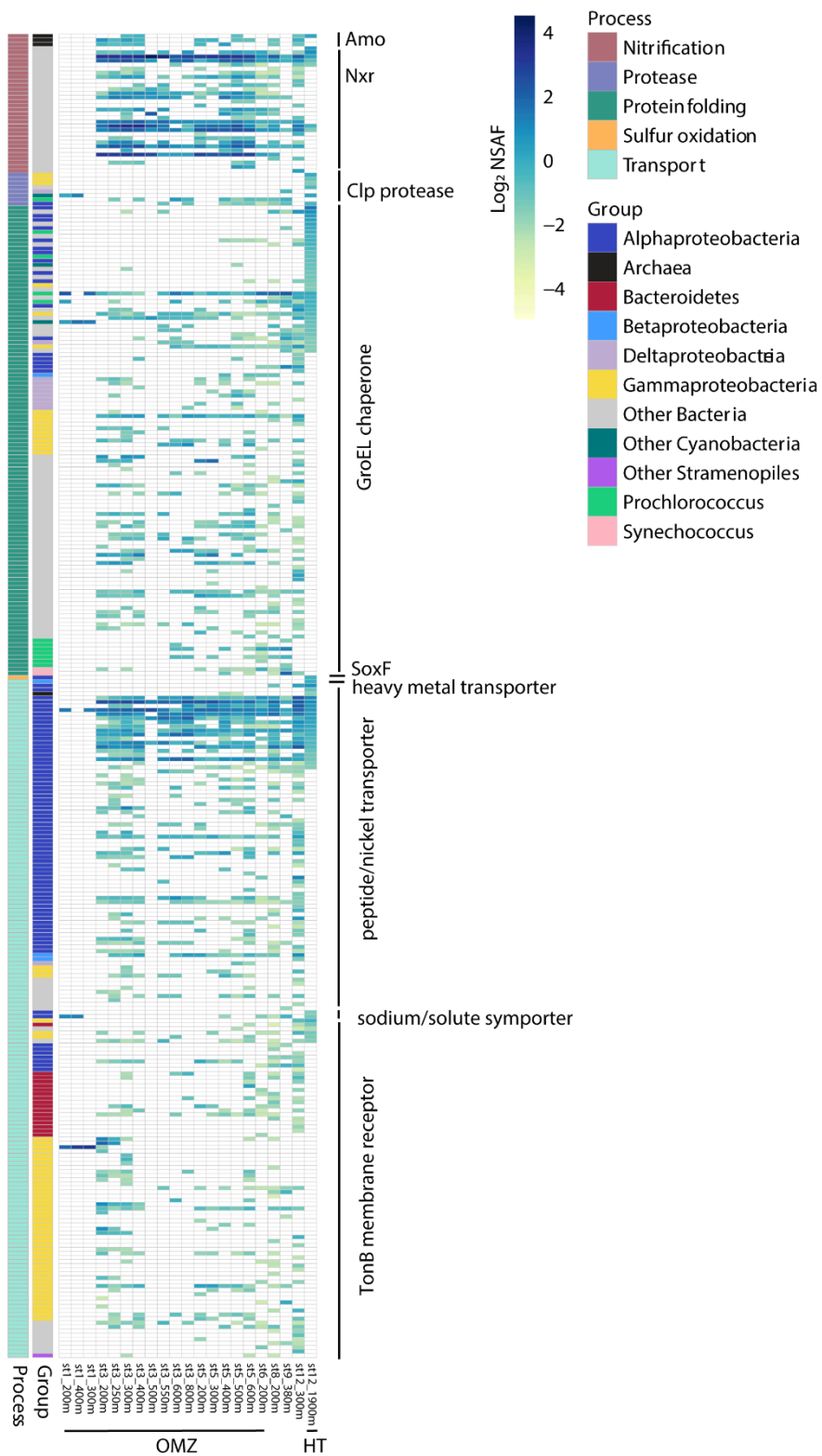
Conclusion & Outlook

655 This study represents the first metaproteomic assessment of deep sea microbial communities in a dispersing hydrothermal plume, and will be valuable in generating hypotheses regarding hydrothermal plume carbon cycling, food web structure, and metabolic plasticity of deep sea microbial communities. There are several recommendations that can be made for future studies evaluating microbial metabolism in distal plume environments: 1) Performing meta-'omics on distal plumes is challenging, and real-time tracking of hydrothermal features onboard the research vessel is recommended to ensure optimal locations and

660 depths are sampled. Meta-'omic analyses in future studies will benefit from sample collection guided by *in situ* optical and redox sensors to maximize the biological signal that might be expected from samples taken toward the plume core. For example, investigations into metaproteomes of microbes residing in a metal-rich plume's center may reveal additional metal uptake, oxidation, or efflux proteins and processes not identified here. 2) In this study, we focused on particle-associated bacteria and protists collected onto 3-51 μm filters. These findings may differ from the functionality of pelagic bacteria (<3

665 μm) inhabiting hydrothermal plume environments. It is therefore recommended to survey both communities in future studies to ensure a comprehensive assessment of plume dynamics. 3) Finally, differences in taxonomic composition of microbial communities between hydrothermally-influenced sites and background seawater were not observed using the 16S/18S rRNA amplicon sequencing and metaproteomic approaches described here, although communities may be taxonomically distinct at a lower classification level. In particular, longer target regions and greater sequencing depth could provide enhanced resolution

670 revealing differences in genera, species or strains.

In summary, trace metal distributions along the central Pacific Ocean reflect a combination of biogeochemical influences, including biological uptake in surface waters, dissolution and decreased metal oxide production in OMZs, heterotrophic remineralization, scavenging at depth, and hydrothermal inputs. In the NE Lau Basin, several distinct hydrothermal plumes

675 sourced from local spreading centers or volcanoes were observed. Hydrothermal dFe and dMn escapes into the tropical southwest Pacific in distal plumes, transporting metals to the surrounding bathypelagic ecosystem with a dFe:^{3}He ratio that rivals that of the Lo'ihi and southern East Pacific Rise distal plumes. The communities within the plume taxonomically resembled that of non-hydrothermal sites, perhaps indicative of background seawater that is entrained into deep sea hydrothermal plumes. Although protein signatures were largely similar between the hydrothermal plume and background

680 locations, there were indications of altered microbial physiology with the differential abundance of proteins involved in metal transport, protein folding, and peptide degradation. The collection of proteins identified here offers a glimpse into hydrothermal vent metabolisms and expands our understanding of biogeochemical processes within basin-scale dispersing hydrothermal plumes and their influences on microbial physiology.

Authors Contributions

685   NRC performed the dissolved trace metal analysis (seaFAST/ICP-MS), analyzed metaproteomic data, and wrote the first draft of the manuscript. AEN processed an early version of the dissolved trace metals data set. TJG, DMM, MRM, MAS, CHL, and NJH collected seawater and protein samples. TJG performed and processed the particulate metal data set, and NJH analyzed dissolved Co. DMM and MRM extracted and generated the metaproteomic data. JPM and AEA generated the 16S rRNA, 18s rRNA, and metatranscriptomic data used to perform peptide spectra matches for the metaproteomic analysis. TJH contributed

690   to intellectual content and interpretations, and CRG contributed to the distal hydrothermal plume interpretations and the writing of the manuscript. CHL and MAS acquired funding for the research expedition and were co-chief scientists. MAS conceptualized, managed the project, and contributed to the writing of the manuscript.

Data Availability

The metaproteomic data has been deposited to the ProteomeXchange Consortium through the PRIDE (Vizcaíno et al., 2013)
695   repository under accession number PXD014230. Dissolved trace metal concentrations have been accepted into the GEOTRACES Intermediate Data Product 2021 and Biological and Chemical Oceanography Data Management Office (BCO-DMO) repositories (https://www.bco-dmo.org/project/2236, https://www.bco-dmo.org/dataset/836347).

Competing Interests

The authors declare that they have no conflict of interest.

700   **Acknowledgements**

References

Agusti, S., J. Gonzalez-Gordillo, D. Vaque, M. Estrada, M. I. Cerezo, G. Salazar, J. M. Gasol, and C. M. Duarte. 2015. Ubiquitous healthy diatoms in the deep sea confirm deep carbon injection by the biological pump. Nat. Commun. **6**: 1–

710   8. doi:10.1038/ncomms8608

Anantharaman, K., J. A. Breier, and G. J. Dick. 2016. Metagenomic resolution of microbial functions in deep-sea hydrothermal
          plumes across the Eastern Lau Spreading Center. ISME J. **10**: 225–239. doi:10.1038/ismej.2015.81

Baars, O., W. Abouchami, S. J. G. Galer, M. Boye, and P. L. Croot. 2014. Dissolved cadmium in the Southern Ocean:
          Distribution, speciation, and relation to phosphate. Limnol. Oceanogr. **59**: 385–399. doi:10.4319/lo.2014.59.2.0385

715   Baker, B. J., R. A. Lesniewski, and G. J. Dick. 2012. Genome-enabled transcriptomics reveals archaeal populations that drive
          nitrification in a deep-sea hydrothermal plume. ISME J. **6**: 2269–2279. doi:10.1038/ismej.2012.64

Baker, E. T., S. L. Walker, G. J. Massoth, and J. A. Resing. 2019. The NE Lau Basin: Widespread and Abundant Hydrothermal
          Venting in the Back-Arc Region Behind a Superfast Subduction Zone. Front. Mar. Sci. **6**: 382.
          doi:10.3389/fmars.2019.00382

720   Beatty, J. T., J. Overmann, M. T. Lince, and others. 2005. An obligately photosynthetic bacterial anaerobe from a deep-sea
          hydrothermal vent. Proc. Natl. Acad. Sci. U. S. A. **102**: 9306–9310. doi:10.1073/pnas.0503674102

Beaulieu, S. E., E. T. Baker, C. R. German, and A. Maffei. 2013. An authoritative global database for active submarine
          hydrothermal vent fields. Geochemistry, Geophys. Geosystems **14**: 4892–4905. doi:10.1002/2013GC004998

Bennett, S. A., E. P. Achterberg, D. P. Connelly, P. J. Statham, G. R. Fones, and C. R. German. 2008. The distribution and
725   stabilisation of dissolved Fe in deep-sea hydrothermal plumes. Earth Planet. Sci. Lett. **270**: 157–167.
          doi:10.1016/j.epsl.2008.01.048

Bennett, S. A., M. Coleman, J. A. Huber, E. Reddington, J. C. Kinsey, C. McIntyre, J. S. Seewald, and C. R. German. 2013.
          Trophic regions of a hydrothermal plume dispersing away from an ultramafic-hosted vent-system: Von Damm vent-site,
          Mid-Cayman Rise. Geochemistry, Geophys. Geosystems **14**: 317–327. doi:10.1002/ggge.20063

730   Biller, D. V., and K. W. Bruland. 2012. Analysis of Mn, Fe, Co, Ni, Cu, Zn, Cd, and Pb in seawater using the Nobias-chelate
          PA1 resin and magnetic sector inductively coupled plasma mass spectrometry (ICP-MS). Mar. Chem. **130**–**131**: 12–20.
          doi:10.1016/j.marchem.2011.12.001

Bostock, H. C., B. N. Opdyke, and M. J. M. Williams. 2010. Characterising the intermediate depth waters of the Pacific Ocean
          using $\delta 13C$ and other geochemical tracers. Deep. Res. Part I Oceanogr. Res. Pap. **57**: 847–859.
735   doi:10.1016/j.dsr.2010.04.005

Bown, J., P. Laan, S. Ossebaar, K. Bakker, P. Rozema, and H. J. W. de Baar. 2017. Bioactive trace metal time series during
          Austral summer in Ryder Bay, Western Antarctic Peninsula. Deep. Res. Part II Top. Stud. Oceanogr. **139**: 103–119.
          doi:10.1016/j.dsr2.2016.07.004

Boyle, E. A., B. A. Bergquist, R. A. Kayser, and N. Mahowald. 2005. Iron, manganese, and lead at Hawaii Ocean Time-series
740   station ALOHA: Temporal variability and an intermediate water hydrothermal plume. Geochim. Cosmochim. Acta **69**:
          933–952. doi:10.1016/j.gca.2004.07.034

Brooks, J. P., D. J. Edwards, M. D. Harwich, and others. 2015. The truth about metagenomics: quantifying and counteracting
          bias in 16S rRNA studies. BMC Microbiol. **15**: 66. doi:10.1186/s12866-015-0351-6

Bruland, K. W., and M. C. Lohan. 2003. Controls of Trace Metals in Seawater, p. 23–47. *In* Treatise on Geochemistry.

745   Chang, C., K. Xu, C. Guo, J. Wang, Q. Yan, J. Zhang, F. He, and Y. Zhu. 2018. PANDA-view: An easy-to-use tool for statistical analysis and visualization of quantitative proteomics data. Bioinformatics **34**: 3594–3596. doi:10.1093/bioinformatics/bty408

Chen, Y., D. Wei, Y. Wang, and X. Zhang. 2013. The role of interactions between bacterial chaperone, aspartate aminotransferase, and viral protein during virus infection in high temperature environment: The interactions between

750   bacterium and virus proteins. BMC Microbiol. **13**. doi:10.1186/1471-2180-13-48

Cohen, N. R., M. R. McIlvin, D. M. Moran, and others. 2021. Dinoflagellates alter their carbon and nutrient metabolic strategies across environmental gradients in the central Pacific Ocean. Nat. Microbiol. doi:10.1038/s41564-020-00814-7

Cowen, J. P., and K. W. Bruland. 1985. Metal deposits associated with bacteria: implications for Fe and Mn marine

755   biogeochemistry. Deep Sea Res. Part A, Oceanogr. Res. Pap. **32**: 253–272. doi:10.1016/0198-0149(85)90078-0

Cowen, J. P., G. J. Massoth, and R. A. Feely. 1990. Scavenging rates of dissolved manganese in a hydrothermal vent plume. Deep Sea Res. Part A, Oceanogr. Res. Pap. **37**: 1619–1637. doi:10.1016/0198-0149(90)90065-4

Cullen, J. T. 2006. On the nonlinear relationship between dissolved cadmium and phosphate in the modern global ocean: Could chronic iron limitation of phytoplankton growth cause the kink? Limnol. Oceanogr. **51**: 1369–1380.

760   doi:10.4319/lo.2006.51.3.1369

Dick, G. J. 2019. The microbiomes of deep-sea hydrothermal vents: distributed globally, shaped locally. Nat. Rev. Microbiol. **17**: 271–283. doi:10.1038/s41579-019-0160-2

Dick, G. J., K. Anantharaman, B. J. Baker, M. Li, D. C. Reed, and C. S. Sheik. 2013. The microbiology of deep-sea hydrothermal vent plumes: Ecological and biogeographic linkages to seafloor and water column habitats. Front.

765   Microbiol. **4**. doi:10.3389/fmicb.2013.00124

Dick, G. J., Y. E. Lee, and B. M. Tebo. 2006. Manganese(II)-oxidizing Bacillus spores in Guaymas basin hydrothermal sediments and plumes. Appl. Environ. Microbiol. **72**: 3184–3190. doi:10.1128/AEM.72.5.3184-3190.2006

Djurhuus, A., S. O. Mikalsen, H. A. Giebel, and A. D. Rogers. 2017. Cutting through the smoke: The diversity of microorganisms in deep-sea hydrothermal plumes. R. Soc. Open Sci. **4**. doi:10.1098/rsos.160829

770   Edgcomb, V. P., S. J. Molyneaux, M. A. Saito, K. Lloyd, S. Böer, C. O. Wirsen, M. S. Atkins, and A. Teske. 2004. Sulfide Ameliorates Metal Toxicity for Deep-Sea Hydrothermal Vent Archaea. Appl. Environ. Microbiol. **70**: 2551–2555. doi:10.1128/AEM.70.4.2551-2555.2004

Fitzsimmons, J. N., E. A. Boyle, and W. J. Jenkins. 2014. Distal transport of dissolved hydrothermal iron in the deep South Pacific Ocean. Proc. Natl. Acad. Sci. **111**: 16654 LP – 16661. doi:10.1073/pnas.1418778111

775   Fitzsimmons, J. N., S. G. John, C. M. Marsay, C. L. Hoffman, S. L. Nicholas, B. M. Toner, C. R. German, and R. M. Sherrell. 2017. Iron persistence in a distal hydrothermal plume supported by dissolved-particulate exchange. Nat. Geosci. **10**: 195–201. doi:10.1038/ngeo2900

Frew, R. D., and K. A. Hunter. 1995. Cadmium-phosphorus cycling at the subtropical convergence south of New Zealand. Mar. Chem. **51**: 223–237. doi:10.1016/0304-4203(95)00057-7

780   Fuchida, S., Y. Mizuno, H. Masuda, T. Toki, and H. Makita. 2014. Concentrations and distributions of amino acids in black and white smoker fluids at temperatures over 200°C. Org. Geochem. **66**: 98–106. doi:10.1016/j.orggeochem.2013.11.008

Garber, A. I., K. H. Nealson, A. Okamoto, S. M. McAllister, C. S. Chan, R. A. Barco, and N. Merino. 2020. FeGenie: A Comprehensive Tool for the Identification of Iron Genes and Iron Gene Neighborhods in Genome and Metagenome
785   Assemblies. Front. Microbiol. **11**. doi:10.3389/fmicb.2020.00037

Gartman, A., and A. J. Findlay. 2020. Impacts of hydrothermal plume processes on oceanic metal cycles and transport. Nat. Geosci. **13**: 396–402. doi:10.1038/s41561-020-0579-0

German, C. R., E. T. Baker, D. P. Connelly, and others. 2006. Hydrothermal exploration of the Fonualei Rift and Spreading Center and the Northeast Lau Spreading Center. Geochemistry, Geophys. Geosystems **7**. doi:10.1029/2006GC001324

790   German, C. R., and W. E. Seyfried. 2013. Hydrothermal Processes, p. 191–233. *In* Treatise on Geochemistry: Second Edition.

Glover, D. M., W. J. Jenkins, S. C. Doney, D. M. Glover, W. J. Jenkins, and S. C. Doney. 2012. Least squares and regression techniques, goodness of fit and tests, and nonlinear least squares techniques, p. 49–74. *In* Modeling Methods for Marine Science.

Goepfert, T. J. 2013. Urea and nickel utilization in marine cyanobacteria as evaluated by incubation, proteomic, and uptake
795   techniques,.

Haalboom, S., D. M. Price, F. Mienis, J. D. L. Van Bleijswijk, H. C. De Stigter, H. J. Witte, G. J. Reichart, and G. C. A. Duineveld. 2020. Patterns of (trace) metals and microorganisms in the Rainbow hydrothermal vent plume at the Mid-Atlantic Ridge. Biogeosciences **17**: 2499–2519. doi:10.5194/bg-17-2499-2020

Hawco, N. J., M. M. McIlvin, R. M. Bundy, and others. 2020. Minimal cobalt metabolism in the marine cyanobacterium
800   Prochlorococcus Proc. Natl. Acad. Sci. **117**: 15740 LP – 15747. doi:10.1073/pnas.2001393117

Herzig, P. M., M. D. Hannington, Y. Fouquet, U. Von Stackelberg, and S. Petersen. 1993. Gold-rich polymetallic sulfides from the lau back arc and implications for the geochemistry of gold in sea-floor hydrothermal systems of the Southwest Pacific. Econ. Geol. **88**: 2182–2209. doi:10.2113/gsecongeo.88.8.2182

Horner, T. J., H. M. Williams, J. R. Hein, M. A. Saito, K. W. Burton, A. N. Halliday, and S. G. Nielsen. 2015. Persistence of
805   deeply sourced iron in the Pacific Ocean. Proc. Natl. Acad. Sci. U. S. A. **112**: 1292–1297. doi:10.1073/pnas.1420188112

Hsu-Kim, H., K. M. Mullaugh, J. J. Tsang, M. Yucel, and G. W. Luther. 2008. Formation of Zn- and Fe-sulfides near hydrothermal vents at the Eastern Lau Spreading Center: Implications for sulfide bioavailability to chemoautotrophs. Geochem. Trans. **9**. doi:10.1186/1467-4866-9-6

Hu, S. K., E. L. Herrera, A. R. Smith, and others. 2021. Protistan grazing impacts microbial communities and carbon cycling
810   at deep-sea hydrothermal vents. bioRxiv 2021.02.08.430233. doi:10.1101/2021.02.08.430233

Huber, J. A., D. B. Mark Welch, H. G. Morrison, S. M. Huse, P. R. Neal, D. A. Butterfield, and M. L. Sogin. 2007. Microbial

population structures in the deep marine biosphere. Science (80-.). **318**: 97–100. doi:10.1126/science.1146689

van Hulten, M., J.-C. Dutay, R. Middag, H. de Baar, M. Roy-Barman, M. Gehlen, A. Tagliabue, and A. Sterl. 2016. Manganese in the world ocean: a first global model. Biogeosciences Discuss. 1–38. doi:10.5194/bg-2016-282

815 Jackson, S. L., J. Spence, D. J. Janssen, A. R. S. Ross, and J. T. Cullen. 2018. Determination of Mn, Fe, Ni, Cu, Zn, Cd and Pb in seawater using offline extraction and triple quadrupole ICP-MS/MS. J. Anal. At. Spectrom. **33**: 304–313. doi:10.1039/C7JA00237H

Jeanthon, C. 2000. Molecular ecology of hydrothermal vent microbial communities. Antonie van Leeuwenhoek, Int. J. Gen. Mol. Microbiol. **77**: 117–133. doi:10.1023/A:1002463825025

820 Jenkins, W. J., S. C. Doney, M. Fendrock, and others. 2019a. A comprehensive global oceanic dataset of helium isotope and tritium measurements. Earth Syst. Sci. Data **11**: 441–454. doi:10.5194/essd-11-441-2019

Jenkins, W. J., M. Hatta, J. N. Fitzsimmons, and others. 2020. An intermediate-depth source of hydrothermal 3He and dissolved iron in the North Pacific. Earth Planet. Sci. Lett. **539**. doi:10.1016/j.epsl.2020.116223

Jenkins, W. J., D. E. Lott, and K. L. Cahill. 2019b. A determination of atmospheric helium, neon, argon, krypton, and xenon
825 solubility concentrations in water and seawater. Mar. Chem. **211**: 94–107. doi:10.1016/j.marchem.2019.03.007

Jickells, T. D., Z. S. An, K. K. Andersen, and others. 2005. Global iron connections between desert dust, ocean biogeochemistry, and climate. Science (80-.). **308**: 67–71. doi:10.1126/science.1105959

John, S. G., J. Helgoe, and E. Townsend. 2018. Biogeochemical cycling of Zn and Cd and their stable isotopes in the Eastern Tropical South Pacific. Mar. Chem. **201**: 256–262. doi:10.1016/j.marchem.2017.06.001

830 Kim, J., S. K. Son, J. W. Son, K. H. Kim, W. J. Shim, C. H. Kim, and K. Y. Lee. 2009. Venting sites along the Fonualei and Northeast Lau Spreading Centers and evidence of hydrothermal activity at an off-axis caldera in the northeastern Lau Basin. Geochem. J. **43**: 1–13. doi:10.2343/geochemj.0.0164

Kogut, M. B., and B. M. Voelker. 2003. Kinetically inert Cu in coastal waters. Environ. Sci. Technol. doi:10.1021/es020723d

Lane, E. S., K. Jang, J. T. Cullen, and M. T. Maldonado. 2008. The interaction between inorganic iron and cadmium uptake
835 in the marine diatom Thalassiosira oceanica. Limnol. Oceanogr. **53**: 1784–1789. doi:10.4319/lo.2008.53.5.1784

Li, J., J. Yang, M. Sun, L. Su, H. Wang, J. Gao, and S. Bai. 2020. Distribution and Succession of Microbial Communities Along the Dispersal Pathway of Hydrothermal Plumes on the Southwest Indian Ridge. Front. Mar. Sci. **7**. doi:10.3389/fmars.2020.581381

Li, M., B. M. Toner, B. J. Baker, J. A. Breier, C. S. Sheik, and G. J. Dick. 2014. Microbial iron uptake as a mechanism for
840 dispersing iron from deep-sea hydrothermal vents. Nat. Commun. **5**: 3192. doi:10.1038/ncomms4192

Little, S. H., C. Archer, A. Milne, C. Schlosser, E. P. Achterberg, M. C. Lohan, and D. Vance. 2018. Paired dissolved and particulate phase Cu isotope distributions in the South Atlantic. Chem. Geol. **502**: 29–43. doi:10.1016/j.chemgeo.2018.07.022

Lupton, J. E., R. J. Arculus, L. J. Evans, and D. W. Graham. 2012. Mantle hotspot neon in basalts from the Northwest Lau
845 Back-arc Basin. Geophys. Res. Lett. **39**. doi:10.1029/2012GL051201

Lupton, J. E., D. G. Pyle, W. J. Jenkins, R. Greene, and L. Evans. 2004. Evidence for an extensive hydrothermal plume in the Tonga-Fiji region of the South Pacific. Geochemistry, Geophys. Geosystems **5**. doi:10.1029/2003GC000607

Lusty, P. A. J., and B. J. Murton. 2018. Deep-ocean mineral deposits: Metal resources and windows into earth processes. Elements **14**: 301–306. doi:10.2138/gselements.14.5.301

850   Marchitto, T. M., W. B. Curry, and D. W. Oppo. 2000. Zinc concentrations in benthic foraminifera reflect seawater chemistry. Paleoceanography **15**: 299–306. doi:10.1029/1999PA000420

Mars Brisbin, M., A. E. Conover, and S. Mitarai. 2020. Influence of Regional Oceanography and Hydrothermal Activity on Protist Diversity and Community Structure in the Okinawa Trough. Microb. Ecol. **80**: 746–761. doi:10.1007/s00248-020-01583-w

855   Martinez, F., B. Taylor, E. T. Baker, J. A. Resing, and S. L. Walker. 2006. Opposing trends in crustal thickness and spreading rate along the back-arc Eastern Lau Spreading Center: Implications for controls on ridge morphology, faulting, and hydrothermal activity. Earth Planet. Sci. Lett. **245**: 655–672. doi:10.1016/j.epsl.2006.03.049

Merino, N., H. S. Aronson, D. P. Bojanova, J. Feyhl-Buska, M. L. Wong, S. Zhang, and D. Giovannelli. 2019. Living at the extremes: Extremophiles and the limits of life in a planetary context. Front. Microbiol. **10**.
860   doi:10.3389/fmicb.2019.00780

Middag, R., H. J. W. de Baar, and K. W. Bruland. 2019. The Relationships Between Dissolved Zinc and Major Nutrients Phosphate and Silicate Along the GEOTRACES GA02 Transect in the West Atlantic Ocean. Global Biogeochem. Cycles **33**: 63–84. doi:10.1029/2018GB006034

Middag, R., S. M. A. C. van Heuven, K. W. Bruland, and H. J. W. de Baar. 2018. The relationship between cadmium and
865   phosphate in the Atlantic Ocean unravelled. Earth Planet. Sci. Lett. **492**: 79–88. doi:10.1016/j.epsl.2018.03.046

Mino, S., H. Maikita, T. Toki, and others. 2013. Biogeography of Persephonella in deep-sea hydrothermal vents of the Western Pacific. Front. Microbiol. **4**: 107. doi:10.3389/fmicb.2013.00107

Mino, S., S. Nakagawa, H. Makita, and others. 2017. Endemicity of the cosmopolitan mesophilic chemolithoautotroph Sulfurimonas at deep-sea hydrothermal vents. ISME J. **11**: 909–919. doi:10.1038/ismej.2016.178

870   Moffett, J. W., and J. Ho. 1996. Oxidation of cobalt and manganese in seawater via a common microbially catalyzed pathway. Geochim. Cosmochim. Acta **60**: 3415–3424. doi:10.1016/0016-7037(96)00176-7

Munson, K. M., C. H. Lamborg, G. J. Swarr, and M. A. Saito. 2015. Mercury species concentrations and fluxes in the Central Tropical Pacific Ocean. Global Biogeochem. Cycles **29**: 656–676. doi:10.1002/2015GB005120

Murdock, S. A., and S. K. Juniper. 2019. Hydrothermal vent protistan distribution along the Mariana arc suggests vent
875   endemics may be rare and novel. Environ. Microbiol. **21**: 3796–3815. doi:10.1111/1462-2920.14729

Muthusamy, S., F. Baltar, J. M. González, and J. Pinhassi. 2014. Dynamics of metabolic activities and gene expression in the Roseobacter clade bacterium Phaeobacter sp. strain MED193 during growth with thiosulfate. Appl. Environ. Microbiol. **80**: 6933–6942. doi:10.1128/AEM.02038-14

Noinaj, N., M. Guillier, T. J. Barnard, and S. K. Buchanan. 2010. TonB-Dependent Transporters: Regulation, Structure, and

880   Function. Annu. Rev. Microbiol. **64**: 43–60. doi:10.1146/annurev.micro.112408.134247

Olsen, B. R., C. Troedsson, K. Hadziavdic, R.-B. Pedersen, and H. T. Rapp. 2015. The influence of vent systems on pelagic eukaryotic micro-organism composition in the Nordic Seas. Polar Biol. **38**: 547–558. doi:10.1007/s00300-014-1621-8

Orellana, L. H., J. K. Hatt, R. Iyer, and others. 2019. Comparing DNA, RNA and protein levels for measuring microbial dynamics in soil microcosms amended with nitrogen fertilizer. Sci. Rep. **9**. doi:10.1038/s41598-019-53679-0

885   Pachiadaki, M. G., E. Sintes, K. Bergauer, and others. 2017. Major role of nitrite-oxidizing bacteria in dark ocean carbon fixation. Science (80-.). **358**: 1046–1051. doi:10.1126/science.aan8260

Rapp, I., C. Schlosser, D. Rusiecka, M. Gledhill, and E. P. Achterberg. 2017. Automated preconcentration of Fe, Zn, Cu, Ni, Cd, Pb, Co, and Mn in seawater with analysis using high-resolution sector field inductively-coupled plasma mass spectrometry. Anal. Chim. Acta **976**: 1–13. doi:10.1016/j.aca.2017.05.008

890   Reed, D. C., J. A. Breier, H. Jiang, and others. 2015. Predicting the response of the deep-ocean microbiome to geochemical perturbations by hydrothermal vents. ISME J. **9**: 1857–1869. doi:10.1038/ismej.2015.4

Reid, J. L. 1997. On the total geostrophic circulation of the Pacific Ocean: Flow patterns, tracers, and transports. Prog. Oceanogr. **39**: 263–352. doi:10.1016/S0079-6611(97)00012-8

Resing, J. A., P. N. Sedwick, C. R. German, W. J. Jenkins, J. W. Moffett, B. M. Sohst, and A. Tagliabue. 2015. Basin-scale
895   transport of hydrothermal dissolved metals across the South Pacific Ocean. Nature **523**: 200–203. doi:10.1038/nature14577

Reveillaud, J., E. Reddington, J. McDermott, and others. 2016. Subseafloor microbial communities in hydrogen-rich vent fluids from hydrothermal systems along the Mid-Cayman Rise. Environ. Microbiol. **18**: 1970–1987. doi:10.1111/1462-2920.13173

900   Rodionov, D. A., P. Hebbeln, M. S. Gelfand, and T. Eitinger. 2006. Comparative and functional genomic analysis of prokaryotic nickel and cobalt uptake transporters: Evidence for a novel group of ATP-binding cassette transporters. J. Bacteriol. **188**: 317–327. doi:10.1128/JB.188.1.317-327.2006

Roshan, S., J. Wu, and T. DeVries. 2017. Controls on the Cadmium-Phosphate Relationship in the Tropical South Pacific. Global Biogeochem. Cycles **31**: 1516–1527. doi:10.1002/2016GB005556

905   Roshan, S., J. Wu, and W. J. Jenkins. 2016. Long-range transport of hydrothermal dissolved Zn in the tropical South Pacific. Mar. Chem. **183**: 25–32. doi:10.1016/j.marchem.2016.05.005

Rudnicki, M. D., and C. R. German. 2002. Temporal variability of the hydrothermal plume above the Kairei vent field, 25°S, Central Indian Ridge. Geochemistry, Geophys. Geosystems **3**. doi:10.1029/2001gc000240

Saito, M. A., A. Dorsk, F. Anton, M. R. Mcilvin, M. S. Rapp, G. R. Ditullio, and D. M. Moran. 2015. Needles in the blue sea :
910   Sub-species specificity in targeted protein biomarker analyses within the vast oceanic microbial metaproteome. Proteomics **00**: 1–11. doi:10.1002/pmic.201400630

Saito, M. A., T. J. Goepfert, A. E. Noble, E. M. Bertrand, P. N. Sedwick, and G. R. Ditullio. 2010. A seasonal study of dissolved cobalt in the Ross Sea, Antarctica: Micronutrient behavior, absence of scavenging, and relationships with Zn, Cd, and

P. Biogeosciences **7**: 4059–4082. doi:10.5194/bg-7-4059-2010

915 Saito, M. A., M. R. McIlvin, D. M. Moran, and others. 2020. Abundant nitrite-oxidizing metalloenzymes in the mesopelagic zone of the tropical Pacific Ocean. Nat. Geosci. **13**: 355–362. doi:10.1038/s41561-020-0565-6

Saito, M. A., M. R. McIlvin, D. M. Moran, T. J. Goepfert, G. R. DiTullio, A. F. Post, and C. H. Lamborg. 2014. Multiple nutrient stresses at intersecting Pacific Ocean biomes detected by protein biomarkers. Science (80-.). **345**: 1173–1177. doi:10.1126/science.1256450

920 Saito, M. A., A. E. Noble, N. Hawco, and others. 2017. The acceleration of dissolved cobalt's ecological stoichiometry due to biological uptake, remineralization, and scavenging in the Atlantic Ocean. Biogeosciences **14**: 4637–4662. doi:10.5194/bg-14-4637-2017

Santoro, A. E., M. A. Saito, T. J. Goepfert, C. H. Lamborg, C. L. Dupont, and G. R. DiTullio. 2017. Thaumarchaeal ecotype distributions across the equatorial Pacific Ocean and their potential roles in nitrification and sinking flux attenuation.
925 Limnol. Oceanogr. **62**: 1984–2003. doi:10.1002/lno.10547

Sheik, C. S., K. Anantharaman, J. A. Breier, J. B. Sylvan, K. J. Edwards, and G. J. Dick. 2015. Spatially resolved sampling reveals dynamic microbial communities in rising hydrothermal plumes across a back-arc basin. ISME J. **9**: 1434–1445. doi:10.1038/ismej.2014.228

Sieber, M., T. M. Conway, G. F. de Souza, H. Obata, S. Takano, Y. Sohrin, and D. Vance. 2019. Physical and biogeochemical
930 controls on the distribution of dissolved cadmium and its isotopes in the Southwest Pacific Ocean. Chem. Geol. **511**: 494–509. doi:10.1016/j.chemgeo.2018.07.021

Sohrin, Y., S. Urushihara, S. Nakatsuka, T. Kono, E. Higo, T. Minami, K. Norisuye, and S. Umetani. 2008. Multielemental determination of GEOTRACES key trace metals in seawater by ICPMS after preconcentration using an ethylenediaminetriacetic acid chelating resin. Anal. Chem. **80**: 6267–6273. doi:10.1021/ac800500f

935 Speer, K., and A. M. Thurnherr. 2012. The lau basin float experiment (LAUB-FLEX). Oceanography **25**: 284–285. doi:10.5670/oceanog.2012.27

Staudigel, H., S. R. Hart, A. A. P. Koppers, C. Constable, R. Workman, M. Kurz, and E. T. Baker. 2004. Hydrothermal venting at Vailulu'u Seamount: The smoking end of the Samoan chain. Geochemistry, Geophys. Geosystems **5**. doi:10.1029/2003GC000626

940 Staudigel, H., S. R. Hart, A. Pile, and others. 2006. Vailulu'u seamount, Samoa: Life and death on an active submarine volcano. Proc. Natl. Acad. Sci. U. S. A. **103**: 6448–6453. doi:10.1073/pnas.0600830103

Sunda, W. G., and S. A. Huntsman. 2000. Effect of Zn, Mn, and Fe on Cd accumulation in phytoplankton: Implications for oceanic Cd cycling. Limnol. Oceanogr. **45**: 1501–1516. doi:10.4319/lo.2000.45.7.1501

Sunda, W. G., S. A. Huntsman, and G. R. Harvey. 1983. Photoreduction of manganese oxides in seawater and its geochemical
945 and biological implications. Nature **301**: 234–236. doi:10.1038/301234a0

Sylvan, J. B., B. M. Toner, and K. J. Edwards. 2012. Life and death of deep-sea vents: Bacterial diversity and ecosystem succession on inactive hydrothermal sulfides. MBio **3**: 1–10. doi:10.1128/mBio.00279-11

Tagliabue, A., L. Bopp, J. C. Dutay, and others. 2010. Hydrothermal contribution to the oceanic dissolved iron inventory. Nat. Geosci. **3**: 252–256. doi:10.1038/ngeo818

950   Takai, K., T. Nunoura, J. I. Ishibashi, and others. 2008. Variability in the microbial communities and hydrothermal fluid chemistry at the newly discovered Mariner hydrothermal field, southern Lau Basin. J. Geophys. Res. Biogeosciences **113**. doi:10.1029/2007JG000636

Takano, S., M. Tanimizu, T. Hirata, K. C. Shin, Y. Fukami, K. Suzuki, and Y. Sohrin. 2017. A simple and rapid method for isotopic analysis of nickel, copper, and zinc in seawater using chelating extraction and anion exchange. Anal. Chim. 955   Acta **967**: 1–11. doi:10.1016/j.aca.2017.03.010

Tebo, B. M., H. A. Johnson, J. K. McCarthy, and A. S. Templeton. 2005. Geomicrobiology of manganese(II) oxidation. Trends Microbiol. **13**: 421–428. doi:10.1016/j.tim.2005.07.009

Templeton, A. S., H. Staudigel, and B. M. Tebo. 2005. Diverse Mn(II)-oxidizing bacteria isolated from submarine basalts at Loihi seamount. Geomicrobiol. J. **22**: 127–139. doi:10.1080/01490450590945951

960   Tivey, M. K. 2007. Generation of seafloor hydrothermal vent fluids and associated mineral deposits. Oceanography **20**: 50–65. doi:10.5670/oceanog.2007.80

Toner, B. M., S. C. Fakra, S. J. Manganini, and others. 2009. Preservation of iron(II) by carbon-rich matrices in a hydrothermal plume. Nat. Geosci. **2**: 197–201. doi:10.1038/ngeo433

Toner, B. M., C. R. German, G. J. Dick, and J. A. Breier. 2016. Deciphering the Complex Chemistry of Deep-Ocean Particles 965   Using Complementary Synchrotron X-ray Microscope and Microprobe Instruments. Acc. Chem. Res. **49**: 128–137. doi:10.1021/acs.accounts.5b00282

VerBerkmoes, N. C., V. J. Denef, R. L. Hettich, and J. F. Banfield. 2009. Systems Biology: Functional analysis of natural microbial consortia using community proteomics. Nat. Rev. Microbiol. **7**: 196–205. doi:10.1038/nrmicro2080

Ward, D. E., K. R. Shockley, L. S. Chang, R. D. Levy, J. K. Michel, S. B. Conners, and R. M. Kelly. 2002. Proteolysis in 970   hyperthermophilic microorganisms. Archaea **1**: 63–74. doi:10.1155/2002/503191

Wei, D., and X. Zhang. 2010. Proteomic Analysis of Interactions between a Deep-Sea Thermophilic Bacteriophage and Its Host at High Temperature. J. Virol. **84**: 2365–2373. doi:10.1128/jvi.02182-09

White, S. N., A. D. Chave, G. T. Reynolds, and C. L. Van Dover. 2002. Ambient light emission from hydrothermal vents on the Mid-Atlantic Ridge. Geophys. Res. Lett. **29**. doi:10.1029/2002GL014977

975   Wilson, S. T., N. J. Hawco, E. V. Armbrust, and others. 2019. Kīlauea lava fuels phytoplankton bloom in the North Pacific Ocean. Science (80-.). **365**: 1040–1044. doi:10.1126/science.aax4767

Wu, J., M. L. Wells, and R. Rember. 2011. Dissolved iron anomaly in the deep tropical-subtropical Pacific: Evidence for long-range transport of hydrothermal iron. Geochim. Cosmochim. Acta **75**: 460–468. doi:10.1016/j.gca.2010.10.024

Wuttig, K., A. T. Townsend, P. van der Merwe, and others. 2019. Critical evaluation of a seaFAST system for the analysis of 980   trace metals in marine samples. Talanta **197**: 653–668. doi:10.1016/j.talanta.2019.01.047

Xie, R. C., S. J. G. Galer, W. Abouchami, M. J. A. Rijkenberg, J. De Jong, H. J. W. De Baar, and M. O. Andreae. 2015. The

cadmium-phosphate relationship in the western South Atlantic - The importance of mode and intermediate waters on the global systematics. Mar. Chem. **177**: 110–123. doi:10.1016/j.marchem.2015.06.011